Optomechanical crystal in light-resilient quantum ground-state

Johan Kolvik,* Paul Burger, David Hambraeus, Trond H. Haug, Joey Frey, Mads B. Kristensen, and Raphaël Van Laer[†]

Department of Microtechnology and Nanoscience (MC2),

Chalmers University of Technology. 41298 Göteborg, Sweden

(Dated: October 20, 2025)

Interaction between light and high-frequency sound is a key area in integrated photonics, quantum and nonlinear optics, and quantum science. However, the typical suspended optomechanical structures suffer from poor thermal anchoring, making them susceptible to thermal noise arising from optical absorption. Here, we demonstrate a chip-scale, release-free silicon optomechanical crystal cavity (OMC) operating cryogenically with improved resilience to laser light. Relative to a suspended nanobeam OMC, we observe an 18 dB suppression of the thermo-optic effect, and the device sustains near-unity phonon occupation at 35 dB higher intracavity optical energy. Time-resolved measurements further reveal rapid initial thermalization governed by the mechanical decay time. With further material and design improvements in sight, these results bolster release-free systems on a chip as a path for low-noise and high-power classical and quantum electro-optomechanics, such as for frequency converters between microwave and optical photons.

I. INTRODUCTION

Nanomechanical systems have emerged as a promising platform for both classical and quantum technologies [1]. The mechanical system can act as a universal bus, efficiently bridging otherwise weakly coupled degrees of freedom such as microwave and optical photons [2]. The silicon optomechanical crystal (OMC) is a compelling gigahertz-frequency nanomechanical system that over the past decade has enabled several key advances, including active ground-state cooling [3-5], microwave-optical entanglement [6, 7], remote mechanical entanglement [8], generation of non-classical states of light [9-11], and mechanical states with second-scale lifetimes [12]. These devices are attractive in the quantum regime, thanks to their strong interaction between light and GHz sound and, in the absence of light, passive initialization in the mechanical ground-state at millikelvin temperatures.

However, further progress is limited by elevated thermal noise arising from optical absorption, a challenge shared across MHz- [13] and GHz-frequency [14, 15] suspended optomechanics. While the original and most common OMC designs use suspended nanobeams to achieve low mechanical dissipation, this also results in thermally isolated structures vulnerable to build-up of thermal noise. Although two-dimensional suspended devices designed to mitigate heating demonstrate promise in both pulsed and continuous-wave operation [4, 16, 17], their noise performance remains a challenge, and they have yet to support quantum experiments combining optical and microwave photons. Another promising approach – although more challenging to scale – involves macroscopic bulk mechanical modes more resistant to laser heating [18]. These limitations highlight the need

to revisit the basic design principles governing the interaction between light and high-frequency sound to enable faster and higher-fidelity quantum optomechanical operations.

In an effort to further improve thermal anchoring in nano-scale optomechanical devices, we recently demonstrated release-free optomechanical crystal cavities that maintain strong mechanical confinement and efficient light-sound interaction even without suspension [19, 20]. This new class of OMCs leverages mechanical modes that are intrinsically protected from radiating into surface and bulk acoustic waves through total internal reflection. At room temperature, these release-free devices showed encouraging optomechanical zero-point coupling rates of $g_{\rm om}/(2\pi) = 0.5\,{\rm MHz}$ and optical (mechanical) quality factors of $2.4\cdot 10^5$ (850) [19].

In this work, we investigate the cryogenic performance of the release-free OMCs, focusing on optical power handling and associated thermal noise. By benchmarking against conventional suspended nanobeam OMCs, we show that the release-free design improves resistance to heating resulting from optical absorption. We begin to show that the thermo-optic effect in our release-free devices activates at around 18 dB higher optical intracavity energy compared to the suspended counterpart. We further characterize thermal noise through single-phononcounting, finding that the release-free device supports optical pump powers up to 35 dB higher than the suspended version when operated at thermal noise occupancy $n_{\rm m} < 1$. The devices thermalize back from high noise levels towards the ground state in a few hundred nanoseconds, speaking for the potential of the release-free approach in high-repetition-rate quantum protocols.

II. RELEASE-FREE OPTOMECHANICAL CRYSTALS

The release-free optomechanical crystal confines GHz sound through the principle of total internal reflection

^{*} kolvik@chalmers.se

[†] raphael.van.laer@chalmers.se

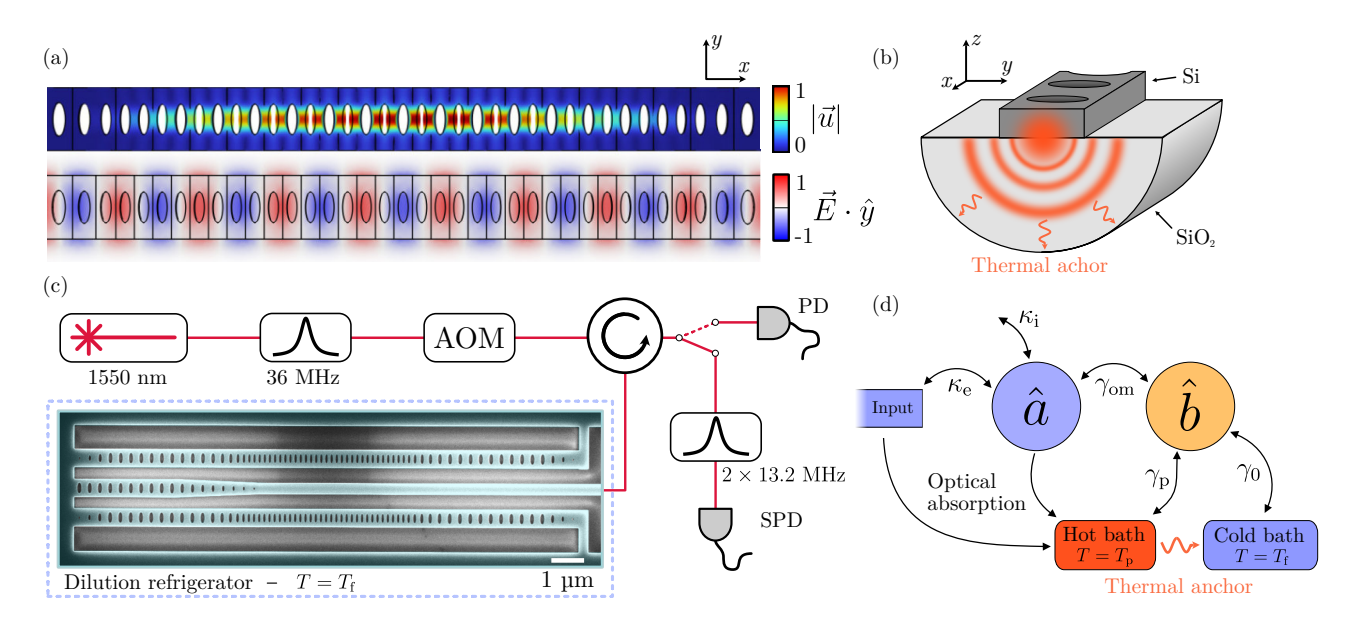


FIG. 1. Release-free optomechanical crystal for improved thermal anchoring. (a) Top-down view of simulated mechanical and optical mode profiles showing normalized displacement \vec{u} and electrical \vec{E} fields respectively. The OMC consists of a defect region with 31 unit cells between two adiabatically tapered mirror regions [19]. (b) The bottom side of the silicon nanobeam is fully attached to the underlying substrate, opening up a channel through which heat can decay. The mechanical mode of interest is protected from leakage by total internal reflection. (c) Simplified phonon-counting setup and a scanning electron micrograph of two release-free OMCs adjacent to an optical bus waveguide. We place the devices in a dilution refrigerator at temperature T_f and study them using a near-infrared laser with a wavelength around 1550 nm. Using acousto-optic modulation (AOM), we send both continuous-wave and pulsed signals to the devices via a circulator. Finally, we measure the reflected light with a photodiode (PD) or through single-photon detection (SPD). The SPD arm singles out optomechanical sidebands by removing pump light with two filter cavities with 13.2 MHz bandwidth. (d) Phenomenological model describing the mechanical environment under optical pumping. The optical mode \hat{a} is populated through an input waveguide with rate $\kappa_{\rm e}$ and decays to the environment through internal losses $\kappa_{\rm i}$. Pumping the optical mode gives rise to the optomechanical interaction that allows phonon-photon exchange at rate $\gamma_{\rm om} = 4g_{\rm om}^2 n_{\rm c}/\kappa$ where $\kappa = \kappa_{\rm i} + \kappa_{\rm e}$ and $n_{\rm c}$ is the number of intracavity pump photons. The mechanical mode \hat{b} is coupled to the hot (cold) thermal bath at rates $\gamma_{\rm p}$ (γ_0) where the cold bath is thermalized to $T_{\rm f}$ and the hot bath to an elevated temperature $T_{\rm p}$ due to optical absorption in \hat{a} and the input waveguide. Enhanced thermal anchoring opens a direct channel for hot bath phonon decay into the cold bath, reducing the thermal load on the mechanical mode.

[19]. The mechanical mode of interest resides near the X-point of the defect-unit-cell's band structure, featuring a pinching-type motion (Fig. 1a). Due to geometrical softening [19, 21], the choice of substrate need not be restricted to materials with higher bulk sound velocity than for the silicon device layer. This enables release-free OMC designs compatible with a wide range of platforms including silicon-on-insulator (SOI) [19] and silicon-onsapphire [20], such that fabrication can be tailored to the needs of the application. The present device is fabricated on SOI with a 220 nm device layer [19] on 2 µm thermal silicon dioxide. Having an entire side of the device in full contact with the chip surface opens up a large area through which thermal noise can dissipate (Fig. 1b). An increased rate of thermal phonon dissipation should allow the OMC to operate at higher applied optical power at a given thermal noise phonon occupancy $n_{\rm m}$.

To analyze the thermal noise in our devices, we consider a phenomenological model for the mechanical mode's thermal environment (Fig. 1d) [14]. The mechanical mode \hat{b} couples to an optical cavity \hat{a} through the

parametrically-enhanced optomechanical scattering rate $\gamma_{\rm om}$ (Fig. 1). In addition to the two coupled oscillators, the model also introduces two thermal baths that couple incoherently to the mechanical mode. The cold bath is the collection of modes that thermalize to the temperature of the surrounding environment $T_{\rm f}$ and interacts with the mechanical mode with the intrinsic decay rate γ_0 . The hot bath on the other hand, is conjectured to be a thermal bath populated by high-frequency phonons thermalized to an elevated temperature T_p [12]. This elevated temperature likely results from optical absorption in electronic defect states present in the etched silicon surfaces [22]. Through nonlinear interactions, the highfrequency thermal phonons would then downconvert and mix with the protected GHz mechanical mode at a rate $\gamma_{\rm p}$ [17]. Optical absorption occurs in all etched silicon surfaces implying that hot bath stimulus can come from both the OMC active region and indirectly via the optical bus waveguide supplying the OMC with light (Fig. 1c,d) [16, 17].

A central aspect of the release-free geometry is the ma-

terial interface between the thin-film silicon and the underlying substrate. The release-free approach relies on the protected mechanical mode being confined on the thin-film side of the interface, whereas thermal noise phonons are not. However, due to the mismatch of material properties at the interface, even the noise phonons may reflect partially [23, 24] resulting in interfacial thermal resistance (ITR). Although theoretical models exist, there appears to be little experimental work on ITR in thin-film structures at cryogenic temperatures. This makes it an open question whether release-free devices can indeed deliver improved thermal handling, or whether their performance is limited by ITR.

In this study, we compare the thermalization properties of a release-free OMC [19] to that of a conventional suspended nanobeam OMC [25]. The devices are fabricated identically apart from that the suspended OMCs undergo a final suspension step before measurement (App. A). The release-free and suspended devices are fixed to the mixing chamber of a dilution refrigerator to allow characterization under varying ambient temperature (App. B). Before delving into the thermal properties, we characterize the optomechanical performance of the devices (App. C). We begin by studying the optical properties by laser spectroscopy. For the release-free OMC, we measure total optical linewidth $\kappa/(2\pi) = 1.63\,\mathrm{GHz}$, and external coupling $\kappa_{\rm e}/(2\pi)=680\,{\rm MHz}$. Next, we measure the optomechanical coupling and mechanical frequency at a dilution fridge temperature of 10 mK. Our cryogenic electromagnetically-induced-transparency (EIT) measurements (App. D) [26] yield a mechanical frequency $\omega_{\rm m}/(2\pi) = 5.358\,{\rm GHz}$ and optomechanical coupling $g_{\rm om}/(2\pi) = 470\,\rm kHz$ for the release-free device.

III. THERMO-OPTIC ROBUSTNESS

In order to investigate the OMCs' thermal properties, we first study the thermo-optic nonlinearity as a simple and approximate indicator of the thermal anchoring. When an OMC heats up due to optical absorption, the silicon's temperature-dependent refractive index causes the optical resonance to redshift [27]. We study this phenomenon by sweeping a tunable laser (Fig. 2a) over the OMC optical mode and recording the resonance frequency shift $\Delta\omega$ as a function of input optical power. Taking into account the strong temperature dependence of the OMC material's thermal properties, we perform the experiment at three different dilution fridge temperatures (Fig. 2b).

At room-temperature, a strong thermo-optic redshift dominates the nonlinear behavior of both suspended and release-free devices. However, we see that the release-free device withstands an order of magnitude higher intracavity optical photons (n_c) at fixed redshift. Now, we repeat the experiment at cryogenic temperatures. The thermo-optic nonlinearity diminishes drastically at lower temperatures [28] which is indicated by the onset of red-

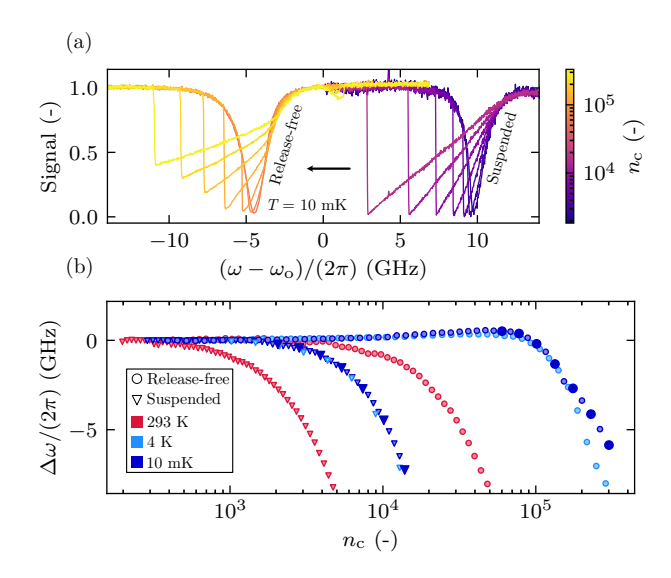


FIG. 2. Suppressed thermo-optic nonlinearity in a release-free optomechanical crystal. (a) Normalized optical reflection recorded at 10 mK where release-free and suspended data is horizontally offset for visual clarity. We record the data while sweeping the laser frequency in a sawtooth pattern with direction indicated by the black arrow. For each optical power we calculate the intracavity photon number n_c achieved at resonant pumping. (b) Optical frequency shift $\Delta\omega$ as function of temperature and intracavity photons n_c . At each power, we extract the optical resonance frequency shift. Bold data points correspond to the curves presented in (a).

shifting at higher optical cavity occupancy for both devices (Fig. 2b). At both 4 K and 10 mK, we measure a greatly increased power stability for the release-free device which now show equal redshift to the suspended device for at least 18 dB increased intracavity photons. We observe additional nonlinearities in the release-free device that activate at $n_c > 10^4$. First of these nonlinearities is a blueshift measured in the range $n_c \in [10^4, 10^5]$ which we attribute to free carrier dispersion [27]. In addition, the high optical occupancies achieved in the release-free device also cause nonlinear losses resulting in diminishing optical extinction ratios (Fig. 2a). An absorptive loss channel such as two-photon absorption would cause additional heat in the OMC, further driving the thermo-optic effect [27]. Finally, we observe an optomechanical sideband at $+\omega_{\rm m}$ relative to the optical frequency at high optical cavity occupancy n_c , which we attribute to mechanical self-oscillations.

The nonlinear behavior of the devices is practically unchanged between 4 K and 10 mK. We attribute this to the vanishing thermal capacity of the devices at low temperatures and the low dilution fridge cooling power at 10 mK. At the high pumping powers required for appreciable nonlinear response, the devices equilibrate at the same final temperature regardless of their initial temperature. Due to the vanishing thermo-optic coefficient at low temperatures [28] we would also see no difference

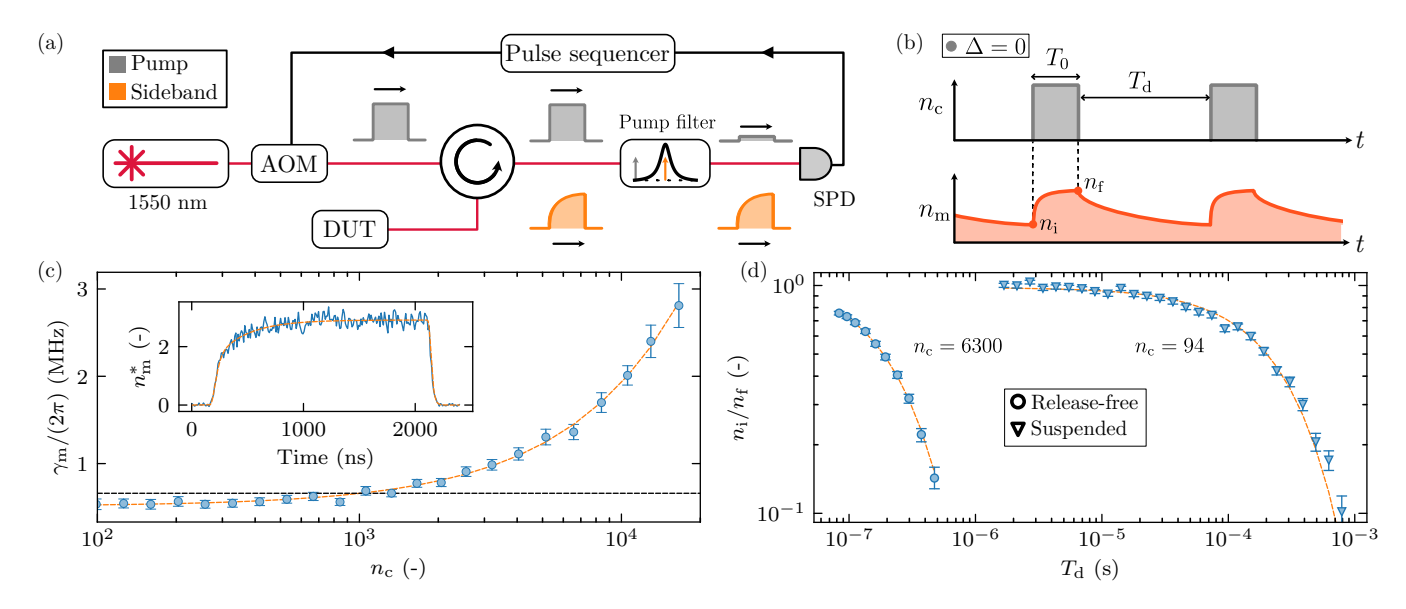


FIG. 3. Thermal noise dynamics of resonantly-driven release-free and suspended OMCs. (a) Simplified schematic of the experimental setup used for pulsed phonon-counting. We illuminate the device under test (DUT) with high extinction ratio optical pulses generated through AOM. Next, we use a set of Fabry-Pérot filters to single out the anti-Stokes sideband at frequency $+\omega_{\rm m}$ relative to the pump. We handle timing between optical pulsing and SPD using a pulse sequencer. (b) The pulse sequence: We drive and read out with resonant pulses of duration T_0 and delay $T_{\rm d}$. Using Eq. (1), we extract initial $(n_{\rm i})$ and final $(n_{\rm f})$ phonon occupation during the optical illumination. (c) Total mechanical linewidth for the release-free device as function of $n_{\rm c}$. We study the dynamics of the scattered optomechanical sideband when illuminating the device with $T_0 = 2 \, \mu s$. For each optical power of the experiment, we fit the collected SPD data (see inset) with Eq. (1) while accounting for filter dispersion to extract the total linewidth with least squares standard deviation. The estimated linewidth agrees with the dark $(n_{\rm c} = 0)$ ringdown result in (d) (black dashed line). Lastly, we fit the linewidth data with a power law (orange dashed line) $\gamma_{\rm m}(n_{\rm c}) = \gamma_0 + \gamma_{\rm p}(n_{\rm c})$, where $\gamma_{\rm p}(n_{\rm c}) = a(n_{\rm c})^b$. (d) Normalized initial phonon occupation versus delay time $T_{\rm d}$ with 95% credibility intervals. We measure exponential decay for both devices, revealing light-off decay rates $\gamma_0/(2\pi) = 660 \, {\rm kHz}$ (528 Hz) for the release-free (suspended) device.

in the thermo-optic response which strengthens this interpretation. Lastly, the increased optical power tolerance of the release-free device indicates that the ITR between the thin-film silicon and the underlying thermal ${\rm SiO}_2$ does not severely limit the thermal capacity of the device even at cryogenic temperatures.

IV. HOT AND COLD BATH COUPLING

To study the noise properties of our devices, we return to the phenomenological model in Fig. 1d. The model suggests that thermal noise in the mechanical mode is governed by its interaction with the hot and cold thermal baths. In this section, we study these interactions at a dilution fridge temperature of 10 mK through pulsed single-phonon-counting with a resonant (detuning $\Delta=0$) optical pump (Methods). We use acousto-optic modulation to generate high-extinction-ratio optical pulses, and use pump filters to selectively measure the anti-Stokes sideband on our SPD (Fig. 3a). For resonant pumping, optomechanical back-action is suppressed which allows for isolated study of the hot and cold bath dynamics ($\gamma_{\rm m}=\gamma_0+\gamma_{\rm p}$) [29]. In addition, we reach higher thermal phonon occupancy at resonant pump-

ing due to higher achievable intracavity optical powers. We use this to study noise dynamics at intermediate phonon occupation levels ($n_{\rm m} \approx 10$). To calibrate the setup, we use sideband asymmetry measured through SPD (App. E).

When exciting the release-free device with 2 µs long resonant square pulses, we measure sideband waveforms with significantly longer rise-times than the input pulses (Fig. 3b). The increased rise time stems from a thermally driven ring-up of the mechanical mode caused by optical absorption in the pump pulse. Assuming that the mechanical mode is coupled to a hot bath at an elevated temperature during optical excitation, we describe the thermal occupation dynamics with

$$n_{\rm m}(t) = n_{\rm i} + (n_{\rm f} - n_{\rm i})(1 - e^{-\gamma_{\rm m}t}), \quad t \in [0, T_0].$$
 (1)

Here, $n_{\rm i}$ is the initial phonon occupation at the start of the pulse and $n_{\rm f}$ is the occupation reached for pulse durations T_0 far exceeding the total mechanical decay rate $\gamma_{\rm m}$. In addition to the dynamics of the mechanical mode, the strong dispersion of the pump filters also leads to distortion in the pulse shape measured by the SPD. We therefore take care to distinguish between the actual time-dependent phonon occupation $n_{\rm m}(t)$ and the measured $n_{\rm m}^*(t)$ in our analysis (App. F,G).

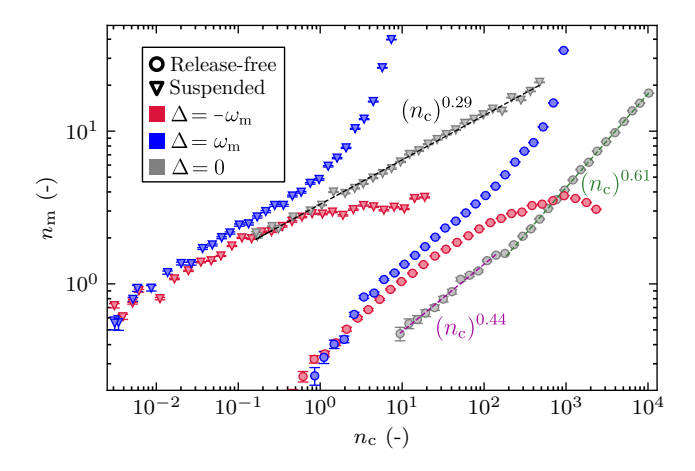


FIG. 4. Single-phonon operation at high continuous-wave optical power at 10 mK. Average mechanical occupation under continuous-wave optical illumination in release-free and suspended OMCs for red, blue and resonant pumping. Data is given with one standard deviation assuming Poissonian statistics for single-photon-counting. To the resonant data, we fit power laws of the form $n_{\rm m}(n_{\rm c}) = \alpha \cdot (n_{\rm c})^{\beta}$, where the different exponents are highlighted in the figure.

Using the noise dynamics model in Eq. (1), we now study the release-free OMC's heating rate at varying optical powers. We fit the measured phonon occupation to Eq. (1) while considering the impact of the filter transfer function to extract $\gamma_{\rm m}(n_{\rm c})$ (Fig. 3c). We see an increase in $\gamma_{\rm m}$ for higher intracavity photons $n_{\rm c}$, and we fit the trend to a power law $\gamma_{\rm m}(n_{\rm c}) = \gamma_0 + \gamma_{\rm p}(n_{\rm c})$, where $\gamma_{\rm p}(n_{\rm c}) = b(n_{\rm c})^a$. From the fit we extract parameters $\gamma_0/(2\pi) = 510 \,\text{kHz}, \, b/(2\pi) = 170 \,\text{Hz} \,\text{and} \, a = 0.98.$ We also show that this $\gamma_{\rm p}(n_{\rm c})$ dependence appears in EIT measurements (App. D). The exponent parameter a is significantly higher than the previously measured 0.29 for two-dimensional devices at high n_c [16, 17]. This higher measured exponent is compatible with a threedimensional ansatz for the hot bath density of states, which predicts a = 1 for $T_p \gg \hbar \omega_{\rm m}/k_{\rm B}$ [12].

In addition, we measure the mechanical decay rate in absence of light by monitoring the ringdown of the thermal mechanical noise for both release-free and suspended devices. We run the test with equal pulse parameters to the previous experiment while setting the power to $n_{\rm c} = 6300 \ (n_{\rm c} = 94)$ for the release-free (suspended) device. We choose the powers of the experiment to achieve $n_{\rm f} \approx 10$ for both devices (Sec. V). Returning to Eq. (1), we extract the initial and final phonon occupation during pulsing and study their dependence on the pulse delay time $T_{\rm d}$ (Fig. 3d). Both devices show exponential decay of the relative initial phonon occupation n_i/n_f with time constants $\gamma_0/(2\pi) = 660 \,\mathrm{kHz} \,(528 \,\mathrm{Hz})$ for the release-free (suspended) device (Fig. 3d). For the release-free device, this value agrees with the low-power result in Fig. 3c and with earlier EIT measurements (App. D).

V. CONTINUOUS-WAVE NOISE THERMOMETRY

With further knowledge of the hot and cold bath couplings (γ_0, γ_p) , we move on to study the thermal occupation of our devices under continuous-wave operation. We extract the average mechanical occupation $n_{\rm m}(n_{\rm c})$ as function of intracavity photons n_c for red, blue and resonant pumping (Fig. 4). As expected, thermal noise generally increases with higher $n_{\rm c}$ for both devices. In addition, off-resonant pumping ($\Delta = \pm \omega_{\rm m}$) yields phonon cooling and amplification due to optomechanical backaction when $\gamma_{\rm om}$ approaches $\gamma_0 + \gamma_{\rm p}$. For resonant pumping, these effects are suppressed leaving thermal driving as the sole contributor to the measured noise occupancy. The mechanical occupancy $n_{\rm m}$ in Fig. 4 represents the total noise in the mechanical mode and differs from the occupation of the hot phonon bath $n_{\rm p}$. In the case of the suspended OMC, we expect a dominant coupling to the hot bath due to the low γ_0 (Fig. 3d) which yields $n_{\rm m} \approx n_{\rm p}$ [12]. However, this assumption does not apply to the release-free device which appears to be predominantly coupled to the cold bath in the range $n_c < 3500$ (Fig. 3c).

We fit the resonant data for both devices to power laws $n_{\rm m}(n_{\rm c})=\beta(n_{\rm c})^{\alpha}$, where we extract $\alpha=0.29$ for the suspended device. This power-law exponent is consistent with the $n_{\rm p}(n_{\rm c})$ dependence previously reported for one-dimensional OMCs, although the proportionality constant β is roughly 2.5 times smaller in this work [12]. For the release-free device, one single power law is not sufficient to describe the resonant data which could be due to its non-trivial noise bath coupling (Fig. 3c). We split up the power law fit into high and low power regions where $\alpha=0.61$, (0.44) for high (low) power regions respectively. Both the low- and high-power exponents measured for the release-free device exceed the $\alpha\approx0.33$ measured for $n_{\rm p}(n_{\rm c})$ in suspended devices [12, 17].

In contrast to the exponent for $\gamma_{\rm p}$, an elevated exponent for $n_{\rm p}(n_{\rm c})$ (α -value) deviates from the prediction of a three-dimensional hot-bath model, which predicts $\alpha=1/(d+1)$ for an effective bath dimensionality d [12]. Therefore, a higher α -value in the region where $\gamma_{\rm p}$ dominates suggests a hot bath exhibiting lower-dimensionality behavior. Deviations of this kind occur also in related quantum devices, where coupling to localized two-level systems (TLS) can alter the phonon dynamics [30, 31]. A complete characterization of such TLS interactions lies beyond the scope of this work. However, we suspect that the etched silicon surfaces and the amorphous SiO₂ of our devices host a reservoir of TLS that can mediate thermal noise between the optical pump and the mechanical mode.

Regarding the noise magnitude, we see a significantly lower thermal occupation for the release-free device for all detunings when compared to the suspended counterpart. At a thermal occupation near $n_{\rm m}=1$, the release-free device withstands 29 dB more intracavity optical energy at

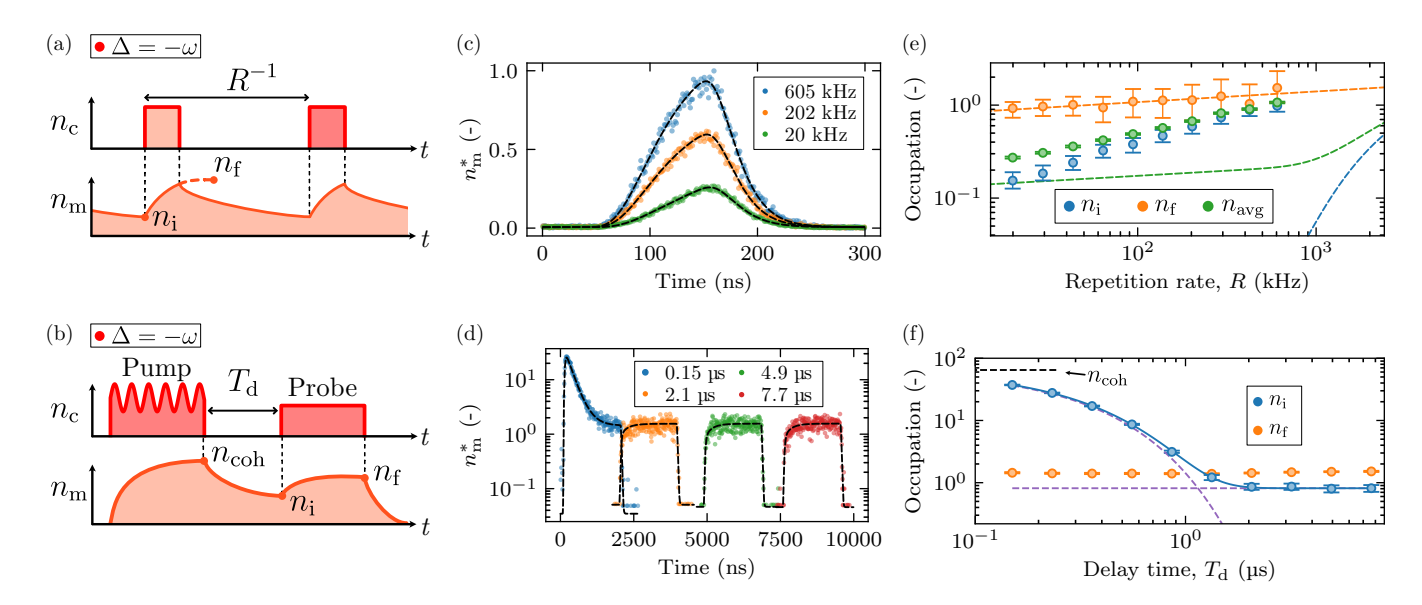


FIG. 5. Off-resonant pulsed noise dynamics of release-free OMC. (a,c,e) Pulse train with 100 ns pulses at $n_c = 128$ for varying repetition rates (R). (b,d,f) Pump-probe experiment for varying probe delay times (T_d) with repetition rate R = 70 kHz, 2 µs pulse durations and $n_c = 48$. (a,b) Pulse schemes. n_i (n_f) is the initial (final) occupation as defined in Eq. (1) whereas $n_{\rm coh}$ is the occupation reached on coherent driving. (c,d) Measured filtered mechanical occupation $(n_{\rm m}^*(t))$ with fits to Eq. (1) with applied filter transfer function. (e) Best fit parameters $[n_i, n_f]$ from (c) together with calculated average phonon occupation $n_{\rm avg}$ with 95% credibility intervals (data points). We include lifetime-limited theory curves (dashed lines) showing the expected noise performance when n_i decays exponentially in between pulses with time constant from Fig. 3d. For this calculation we first fit $n_f(R) = (R/R_0)^\theta$ where $R_0 = 52$ kHz and $\theta = 0.114$. Next we calculate $n_i(T_d) = n_f \exp(-\gamma_0 T_d) + n_0$ where $T_d = R^{-1} - T_0$ and n_0 is the dilution fridge occupation at $T_f = 50$ mK. (f) Best fit parameters $[n_i, n_f]$ from (d) with 95% credibility intervals (data points). We fit the initial occupation to $n_i(T_d) = n_{\rm coh} \exp(-\gamma_{\rm coh} T_d) + n_{\rm res}$ with $n_{\rm coh} = 64$, $\gamma_{\rm coh}/(2\pi) = 607$ kHz and $n_{\rm res} = 0.81$ (blue line). The individual terms of $n_i(T_d)$ are shown as dashed purple lines.

off-resonant pumping compared to the suspended device. For resonant pumping, this increased optical power handling increases to 35 dB. We attribute the increased noise for off-resonant pumping at equal n_c to the bus waveguide providing heat to the OMC through the substrate. We expect the bus waveguide heating to be more prominent for off-resonant pumping due to the higher powers required to reach a certain n_c [16, 17]. The suspended device on the other hand has a less direct thermal link between bus waveguide and OMC which we observe as resonant and off-resonant data converging for low n_c . We therefore expect even lower off-resonant noise for releasefree devices in the absence of bus waveguide heating effects. Despite the higher thermal noise for off-resonant pumping, the optomechanical back-action cools the mechanics for $n_c > 10^3$ (Fig. 4).

For a resonantly pumped cavity, the steady-state mechanical occupation follows from detailed balance as $n_{\rm m}=(\gamma_{\rm p}n_{\rm p}+\gamma_0n_0)/(\gamma_0+\gamma_{\rm p}),$ where n_0 is the occupation of the cold phonon bath (Fig. 1d) [16]. For OMCs where $\gamma_{\rm p}\gg\gamma_0$, we have $n_{\rm m}\approx n_{\rm p}$ if assuming a cold dilution fridge bath. As mentioned above, this does not apply to the release-free device due to the stronger coupling to the cold bath γ_0 . The resonant release-free $\gamma_{\rm m}(n_{\rm c})$ reveals that $\gamma_{\rm p}<\gamma_0$ for $n_{\rm c}<3500$ (Fig. 3c). Therefore, the mechanical mode is predominantly coupled through γ_0 to the cold bath at low $n_{\rm c}$. Nevertheless, the resonant oc-

cupation levels measured for low n_c (Fig. 4) corresponds to a bath temperature of $T_{\rm f} > 200\,{\rm mK}$ which far exceeds the steady state dilution fridge temperatures around 10 mK at low applied optical powers. This appears to be inconsistent with the thermal environment model (Fig. 1d) under the assumption of a cold bath properly thermalized with the 10 mK cryostat. One hypothesis is that the immediate environment of the OMC - representing the cold bath – is at a higher temperature than the dilution fridge due to insufficient thermal transport away from the device. Another hypothesis is that a higher thermal occupation at low n_c might still come from the hot bath if $\gamma_{\rm p}(n_{\rm c})$ includes a low exponent term that would dominate at low n_c – which is not excluded by our data (Fig. 3c). Finally, there may be additional noise sources not currently included in the thermal model (Fig. 1d), such as the TLS ensembles suggested by the lower-dimensionality behavior of the noise scaling at high n_c (Fig. 4).

VI. NOISE OCCUPANCY IN PULSED OPERATION

We now return to pulsed measurements to characterize noise occupancy for off-resonant pumping. With detuning $\Delta = \pm \omega_{\rm m}$ an experiment can be configured to activate beam-splitter or two-mode-squeezing interactions,

both relevant for quantum protocols [29, 32, 33]. In the following, we choose to pump red-detuned to avoid vacuum fluctuations, focusing on the thermal noise aspect.

We first run a short pulse $(T_0=100\,\mathrm{ns}$ experiment with power $(n_\mathrm{c}=128)$ to reach an anti-Stokes scattering rate $p_\mathrm{as}=\gamma_\mathrm{om}T_0=0.05$ (Fig. 5a,c,e). These short and low-scattering-rate pulses are of interest for e.g. heralding experiments [6, 7, 32–34]. We proceed as in our previous pulsed experiments (Sec. IV) to gather data and fit for $[n_\mathrm{i},n_\mathrm{f}]$ with which we here calculate the average phonon occupancy during a pulse as $n_\mathrm{avg}=T_0^{-1}\int n_\mathrm{m}(t)dt$. By repeating the experiment for different delay times T_d , we study the noise in each pulse as a function of the experiment's repetition rate $R=(T_0+T_\mathrm{d})^{-1}$.

The noise dynamics observed in this experiment differ markedly from those in our previous decay measurements (Fig. 3d). Contrary to the expected outcome, the initial occupation (n_i) behaves non-exponentially across the explored repetition rates. In addition, the estimated final occupation (n_f) also scales with repetition rate, suggesting a thermal build-up effect connected to the average dissipated optical power. With this measured performance, the release-free device can be operated under present experimental condition with $n_{\rm avg} < 0.5$ at $R = 100 \,\mathrm{kHz}$, limited by the slow decay of the initial population. This repetition rate (R-value) exceeds the decay rate of state-of-the-art superconducting qubits operating at 5 GHz [35]. When simulating n_{avg} under the assumption of an exponentially-decaying n_i with the intrinsic dynamics measured in Fig. 3d, we estimate that the release-free device could perform quantum experiments with $n_{\rm avg} < 0.3$ for repetition rates exceeding $R = 1 \,\mathrm{MHz}.$

Non-exponential noise dynamics as a function of repetition rate as seen in Fig. 5e have also been reported for two-dimensional suspended OMCs [4], although its origin remains unclear. To study this in more detail, we perform a second red-detuned experiment with a pump-probe pulse scheme (Fig. 5b,d,f). The pump is chosen to be a 2 µs red-detuned pulse with amplitude modulation at the mechanical frequency. The modulated pump drives the mechanical mode into a coherent state with coherent occupation $n_{\rm coh}$ which decays freely after the end of the pump pulse. After a variable decay time $T_{\rm d}$, we read out the mechanical state with a 2 µs probe pulse. For all delay times, the repetition rate of the experiment is fixed to $R=70\,{\rm kHz}$ and both pulses have optical cavity occupancy $n_{\rm c}=48$.

From the extracted initial occupations, we estimate that the pump pulse drives the mechanical mode into a coherent state with $n_{\rm coh}=64$, after which it decays exponentially with a time constant consistent with that obtained in our resonant pulse measurements (Fig. 3d). For delays $T_{\rm d}>2\,\rm \mu s$, however, the decay saturates at $n_{\rm m}\approx0.8$. This saturation level depends on the experiment's repetition rate (App. I) and follows a trend similar to that of the short-pulse occupations (Fig. 5e). We therefore conclude that the mechanical mode decays

freely until reaching a limit set by a slowly decaying reservoir, whose population depends on the average optical power dissipated during the experiment. The decay of this reservoir determines the noise occupancy observed in Fig. 5e. Although the origin and dynamics of this reservoir are not yet fully understood, it may be linked to the elevated continuous-wave noise (high $T_{\rm f}$) observed at low $n_{\rm c}$ (Fig. 4), suggesting a non-exponential decaying cold bath (Sec. V). Finally, we note that this bath remains spatially confined, as the mixing-chamber temperature never exceeded 20 mK during the measurements in this section.

VII. DISCUSSION

In this first-generation device, the release-free OMC withstands nearly two orders of magnitude higher optical power before thermo-optic nonlinearities appear, and it maintains near-unity phonon occupancy at three orders of magnitude higher optical power than suspended nanobeams. Together, these features make the release-free OMCs a promising platform that combines high resilience to optical power with reduced fabrication complexity and fast ground-state thermalization. These results advance the light-resilience of chip-scale mechanical systems operating in the quantum regime.

Time-resolved measurements show that the release-free device rethermalizes rapidly after optical excitation, with initial dynamics governed by the intrinsic mechanical decay time. We also observe thermal noise exhibiting a non-exponential decay, possibly arising from limited chip-to-cryostat heat transport, residual interfacial thermal resistance, or coupling to localized two-level systems. Similar non-exponential behavior reported in two-dimensional suspended OMCs [4] points to a shared underlying mechanism. Under continuous-wave drive, the observed noise scaling also indicates the involvement of lower-dimensional fluctuators such as two-level systems resulting from surface and material defects.

Looking ahead, release-free and light-resilient OMCs provide an appealing platform for investigating noise dynamics in greater depth. Further improvements in surface passivation and chip-to-cryostat thermalization could reduce residual noise levels, while statistical analysis of the noise scaling can give insight into potential effects of fabrication-disorder on thermalization [17]. Regarding optomechanical performance, decreasing the optical mode volume - currently exceeding that of the mechanical mode [19, 20] - would enhance the singlephoton optomechanical coupling strength. Transferring the architecture to a sapphire substrate is a natural next step for release-free OMCs [20]. The sapphire substrate would further improve thermal conductivity, enable the removal of amorphous oxides that host TLS ensembles. and allow direct integration with high-quality superconducting microwave circuits by adding capacitive [36] or piezoelectric [6, 7] elements in a fully release-free electrooptomechanical platform [20].

With respect to applications, the release-free OMCs' combination of high coupling and resilience to optical power opens new avenues for on-chip electro-optomechanics. Experiments such as high-repetition-rate spontaneous down-conversion [4], optomechanically generated single photons [11], microwave-optical entanglement [6, 7, 34, 36, 37], and qubit readout and control [38–41] appear within reach. More broadly, harnessing GHz phonons as coherent intermediaries could enable efficient, low-noise interfaces that connect optics, microwaves, and solid-state systems – including spins, liquids, and superconducting qubits – for emerging technologies in quantum communication, sensing, and computation.

ACKNOWLEDGMENTS

We thank W. Wieczorek, N. J. Engelsen, P. Delsing, O. J. Painter, A. H. Safavi-Naeini and W. Jiang for helpful discussions. The devices were fabricated in the My-Fab Nanofabrication Laboratory at Chalmers. We acknowledge support from the Knut and Alice Wallenberg foundation through the Wallenberg Centre for Quantum Technology through a WACQT Fellowship, from the European Research Council via Starting Grant 948265, and from the Swedish Foundation for Strategic Research via grant FFL21-0039. M. B. K. is supported by the Carlsberg Foundation, Internationalization Fellowship grant CF24-0448.

METHODS

Single-phonon counting. Throughout this study, we characterize the optically-induced thermal noise in our devices through single-phonon counting [15, 42]. This method involves the use of single-photon detectors (SPDs) to measure optomechanically scattered sideband photons as a gauge for the average mechanical occupation. When placing a pump laser in the vicinity of the OMC optical resonance, we selectively measure Stokes or anti-Stokes scattered photons by placing a pair of narrowband tunable Fabry-Pérot filters (13.6 MHz individual bandwidth) over the desired sideband (App. B). At dilution refrigerator temperatures, the gigahertz mechanical mode of our devices is inherently close to its motional ground state. In this regime, the mechanical vacuum fluctuations cause a measurable asymmetry in the amplitude of the optomechanically scattered sidebands [43]. When the pump laser frequency (ω_l) is placed with a detuning $\Delta := \omega_l - \omega_o = \pm \omega_m$ from the optical resonance frequency (ω_0) , the rate of detected sideband photons is

$$\Gamma_{\pm}(t) = \gamma_{\text{om}}(t)\eta_{\text{tot}}\left(n_{\text{m}}(t) + \frac{1}{2}(1\pm 1)\right) + \Gamma_{\text{noise}}(t), (2)$$

for Stokes (+) and anti-Stokes (–) process' respectively. In Eq. (2) we have that $\gamma_{\rm om}(t)=4g_{\rm om}^2n_{\rm c}(t)/\kappa$, $\eta_{\rm tot}$ is the total sideband photon detection efficiency and $n_{\rm m}(t)$ is the average mechanical occupancy. The noise term $\Gamma_{\rm noise}(t)$ comprises both excess laser noise and external noise from dark counts and blackbody radiation (App. H). Eq. (2) provides a direct way to measure thermally excited phonons in both continuous-wave and pulsed measurements. When pumping resonantly, both processes are suppressed by the optical density of states causing a reduction in the detected photon rate by a factor $(\kappa/2\omega_{\rm m})^2$.

Appendix A: Fabrication

For fabricating both release-free and suspended OMCs, we use SOI wafers (SOITEC, $\sigma > 750\,\Omega\,\mathrm{cm}$) with 220 nm device layer and 2 µm buried oxide. We define the OMC pattern with ARP6200 resist and electron-beam lithography (Raith EBPG5200) and transfer it to the device layer with an HBr and Cl₂-based ICP-RIE etch. Following dry-etch, we clean the chips using a piranha solution (3:1, $\mathrm{H_2SO_4:O_2H_2}$) and 2% HF. Finally, the conventional nanobeam OMC chips are suspended in 5% HF.

Appendix B: Experimental setup

In this section, we describe the experimental setup used in this work (Fig. 6). For the laser source, we use a tunable external cavity diode laser (Toptica CTL 1550). While the power of the laser is stabilized internally, we use optical switches to route the laser into a stabilization module for external frequency control. In the stabilization module, we use the Pound-Drever-Hall technique to lock the laser frequency to a fiber coupled Fabry-Pérot filter (LUNA FFP-I, bandwidth = 36 MHz). The transmission frequency of the filter is tuned and stabilized through temperature control (Thorlabs TED200). This lock serves to stabilize the laser during long singlephoton counting experiments in addition to suppressing phase noise and spontaneous emission amplitude noise at the mechanical frequency, crucial for accurate phonon thermometry [43].

After stabilization, we use optical switches to reroute the laser into laser modulators. Pulse modulation is achieved with a pair of 110 MHz acousto-optic modulators (G&H Fiber Q), actuated through microwave drivers by a pulse sequencer module (QM OPX). With this setup, we synthesize pulses with 10-90% rise time of 14 ns and extinction ratio > 100 dB. Electro-optic amplitude modulation is used for EIT (App. D), coherent mechanical driving (App. E) and pump filter alignment. For experiments with amplitude modulated pulses, we drive the EOM with a QM local oscillator unit controlled by the OPX. We send the pre-treated light through a circulator to the device under test placed in our dilution refrig-

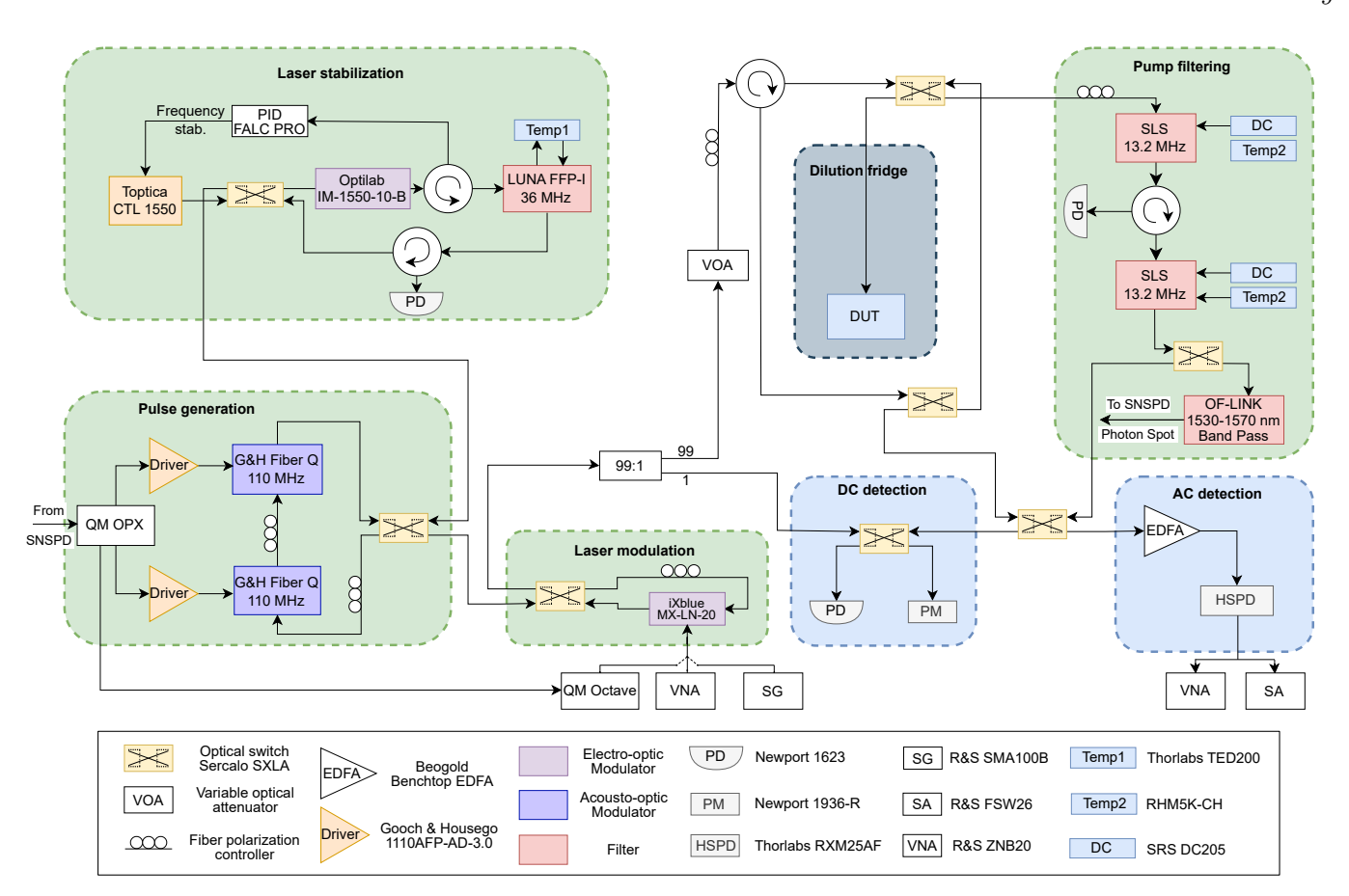


FIG. 6. Experimental setup. We use a Toptica CTL 1550 to perform the studies presented in this work. We lock the laser frequency to a temperature tunable Fabry–Pérot filter with the Pound-Drever-Hall technique. This stabilization also serves to suppress laser phase noise at the mechanical frequency. Before sending the light to the device, we can apply acousto- and electro-optic modulation through in-path switching. The acousto-optic modulation is driven by a Quantum Machines OPX unit which handles sequencing of pulsing and single-photon detection. After preparing the laser light, we send it to the device under test (DUT) which is mounted to the mixing chamber of a dilution refrigerator. We choose to send the reflected light to either linear AC/CD detection using standard photodiodes, or to a single-photon counting path. Before detection, we use a set of two 13.2 MHz wide tunable Fabry–Pérot filters to remove pump light and transmit the optomechanical sideband. Lastly, we suppress stray infrared radiation using a wide band pass filter before sending the light to superconducting nanowire single-photon detectors (SNSPD) operating at the 900 mK stage of the cryostat.

erator system (Bluefors LD400). Before every cooldown, we pre-align to the OMC device using Attocube cryogenic piezo actuation stages. Alignment to the correct device is maintained throughout cryostat cooldown with an automated realignment scheme run every 30 minutes.

Depending on the current measurement, we direct the light reflected off the DUT to either linear or single-phonon detection paths. In the linear detection path, we use a photodetector (Newport 1623) and power meter (Newport 1936-R) for DC characterization and a high-speed photoreceiver (Thorlabs RXM25AF0) for AC sideband detection. In the single-photon detection path, the light passes through two fiber coupled filter cavities (Stable Laser Systems) to remove pump light. The Fabry-Pérot filters have 13.2 MHz bandwidth and 18.8 GHz FSR and provide 114 dB pump suppression at 5 GHz detuning when assembled in series. Next, we run the light through a broadband IR filter (OF-LINK Band Pass) to suppress

unwanted photons outside the C-band before detection. We detect the transmitted sideband on superconducting nanowire singe-photon detectors (SNSPD) (Photon Spot) with output routed to the OPX for photon counting and pulse sequencing.

Because of the very weak signals in the single-photon detection regime, active locking of the pump filters is not feasible. Instead, we use a reference sideband at the mechanical frequency, generated by our EOM, to align the filters to the correct detuning. Filter alignment during measurements is maintained through passive stabilization, combining acoustic and thermal isolation with resistive heater-based temperature control. For longer measurement runs, the filter stack is automatically realigned at intervals of 1–10 minutes. To suppress noise counts on the SNSPDs, the fiber linking the pump filter output to the dilution-fridge input is optically isolated by wrapping it in aluminum foil, and measurements are

TABLE I. Optomechanical properties at 10 mK for the studied devices.

Device	$\omega_{\rm o}/(2\pi)~({ m THz})$	$\omega_{\rm m}/(2\pi)~({\rm GHz})$	$\kappa/(2\pi)$ (GHz)	$\kappa_{\rm e}/2\pi~({ m MHz})$	$\gamma_0/(2\pi)$ (kHz)	$g_{\rm om}/(2\pi)~({\rm kHz})$	Experiment
Release-free	194.5867	5.358	1.63	680	500	470	All
Suspended A	195.6301	5.984	1.35	580	-	855	Thermo-optics
Suspended B	195.7751	5.983	1.70	1030	0.5	1069	Noise thermometry

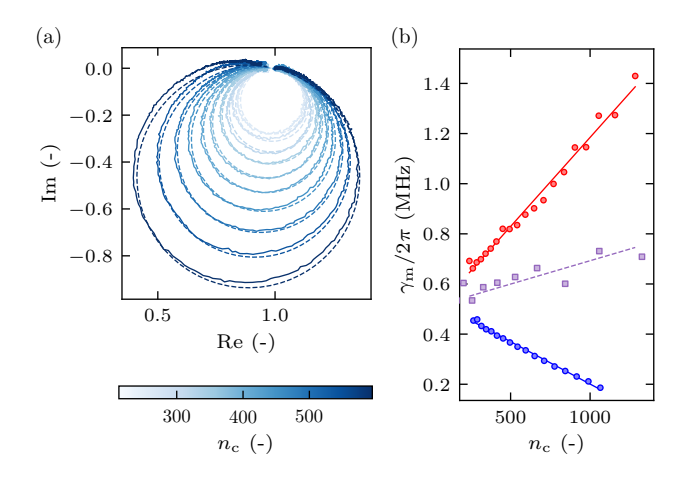


FIG. 7. Release-free electromagnetically induced transparency at 10 mK. (a) Normalized transparency window traces with fits to Eq. (D1). (b) Total mechanical linewidth as function of n_c . Red and blue points are extracted from fits to EIT data, while purple points are taken from Fig. 3b of the main text. Red and blue solid lines are linear fits to the corresponding data sets revealing a slight asymmetry to the slopes. Averaging the linear fits yields the dashed purple line which follows the resonant data with good agreement, revealing the source of the asymmetry to be power dependent hot bath coupling.

performed under minimal ambient light.

Appendix C: Device properties

A full list of device properties is presented in Tab. I. All properties are measured at an ambient temperature of around 10 mK. The study includes one release-free and two suspended OMCs with identical fabrication processes besides the final release step for the suspended devices. The two suspended devices are featured in different parts of the main text data. The thermo-optic effect was studied with suspended device A whereas the single-phonon-counting experiments were performed on suspended device B.

Appendix D: Electromagnetically induced transparency

Due to the low mechanical occupancy in the GHz mechanical modes at millikelvin temperatures the thermomechanical signature on the optical field is weak com-

pared to room temperature. Using thermally-scattered sidebands for cryogenic study of optomechanical effects therefore requires high SNR measurements techniques such as balanced heterodyne detection [14, 16] or single photon detection [6, 8, 12, 15, 16]. On the contrary, *Electromagnetically Induced Transparency* (EIT) [26] exploits coherently driven mechanical excitations for signal generation, thus making it independent of thermal population. In addition, OMC optical stability is often enhanced at low temperatures due to the suppressed thermo-optic effect. This makes EIT appealing for optomechanical backaction characterization at millikelyin temperatures.

We perform EIT measurements by placing an optical pump at blue or red motional sidebands of the OMC optical resonance. A weak sideband is then generated through electro-optic amplitude modulation driven by a vector network analyzer (VNA). We scan the modulation frequency while monitoring the optical reflection on a highspeed photodetector. A transparency feature around the mechanical frequency is measured with the VNA and can be described by a Lorentzian in the complex plane [44]

$$S(\delta\omega) = 1 - \frac{A}{i\delta\omega - \gamma_{\rm m}/2}.$$
 (D1)

In Eq. (D1), we have assumed a modulation frequency $\omega_{\text{mod}} = \omega_{\text{m}} + \delta \omega$ where $\delta \omega \ll \kappa$ and use $A \in \mathbb{C}$ as a fitting parameter. In addition, Eq. (D1) is obtained in the resolved-sideband regime and when normalizing to the response when $\delta \omega \gg \gamma_{\text{m}}$.

We measure VNA traces for the release-free device taken at 10 mK when pumping on the blue motional sideband (Fig. 7a). Fitting the data with Eq. (D1) yields back-action curves for both detunings. We notice a slight asymmetry in the linear slopes for red and blue sides causing disagreement when using the data to calculate optomechanical coupling. Adding the linewidth data extracted from resonant pulsing (Fig. 3b) to the same plot reveals the origin of the asymmetry to be the power dependent hot bath coupling $\gamma_{\rm p}(n_{\rm c})$. We find that the average of the linear curves used to fit the EIT data fits well to the resonant pulsed data as is expected due to the lack of backaction for resonant pulsing.

Appendix E: Thermometry calibration

Performing high-quality thermometry experiments requires precise and reliable calibration of the measured mechanical occupation. Using Eq. (2) as a starting point,

the problem of calibrating the phonon counting setup can be formulated as finding $\Gamma_{\rm cal}$ such that

$$n_{\rm m} = \frac{\Gamma_{\pm}}{\Gamma_{\rm cal} n_{\rm c}} - \frac{1}{2} (1 \pm 1),$$
 (E1)

where Γ_{\pm} is the rate of detected Stokes (+) anti-Stokes (-) photons. $\Gamma_{\rm cal}$ can thus be thought of as being the anti-Stokes detection rate at unit intracavity photon and phonon numbers. In this work, we explore three methods of measuring $\Gamma_{\rm cal}$ based on different principles. In the following, we describe each method and assess its advantages and limitations.

Direct calibration is the simplest of the three methods but requires full knowledge of OMC optomechanical properties and system detection efficiency. In the absence of noise, Eq. (2) immediately yields

$$\Gamma_{\rm cal}^{\rm direct} = \frac{4g_{\rm om}^2 \eta_{\rm tot}}{\kappa},$$
(E2)

where we have assumed anti-Stokes scattering for simplicity. In our setup, the total efficiency can be broken up in $\eta_{\rm tot}=\eta_{\rm o}\eta_{\rm fc}\eta_{\rm loss}\eta_{\rm det},$ where $\eta_{\rm o}=\kappa_{\rm e}/\kappa$ is the optical coupling, $\eta_{\rm fc}$ is the fiber-chip coupling, $\eta_{\rm loss}$ represent photon loss from chip to detectors and η_{det} is the detection efficiency. To calculate this calibration rate, we start by measuring the photon loss from the mixing chamber to the SNSPD input at room temperature. Next, we measure the fiber-chip coupling when the cryostat is cold by comparing the device reflected light to the input. The detection efficiency of the SNSPDs is measured by sending light with known power to the detectors and measuring the recorded click rate. Finally, we measure the optomechanical device properties when the cryostat is cold (Sec. II). Even though simple in nature, the extensive prior system knowledge required leads us to use this calibration method as a cross-check for the following techniques.

Sideband asymmetry. At zero average mechanical occupation, the mechanical resonators ability to emit energy is completely suppressed; however, due to the vacuum fluctuations still present in the resonator, scattering events resulting in phonon absorption are still possible [43]. This is the principle which governs the asymmetry in Stokes/anti-Stokes scattering rates at low phonon occupations as seen in Eq. (E1). We exploit this by measuring the photon detection rate for both Stokes (Γ_+) and anti-Stokes (Γ_-) scattering to calculate

$$\Gamma_{\rm cal}^{\rm asym} = \frac{\Gamma_+ - \Gamma_-}{n_{\rm c}}. \tag{E3}$$

We measure the sidebands while pumping off-resonantly to achieve stronger signals at lower $n_{\rm m}$. For both red and blue detuning, we use the pump filters to scan over the sideband resonant with the OMC optical mode. To accurately place the pump filters at an arbitrary detuning $\Delta_{\rm p}$, we use electro-optic modulation to drive a reference sideband at the desired detuning to which we align the

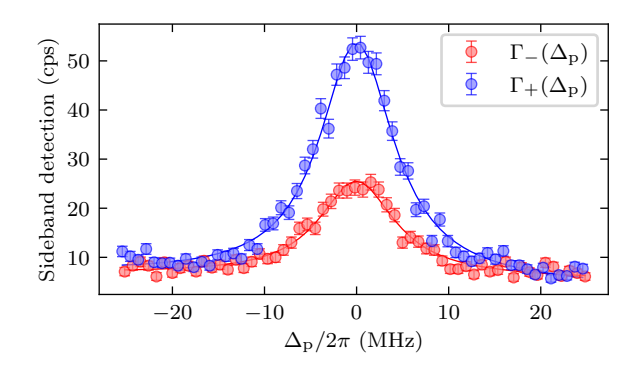


FIG. 8. Sideband asymmetry detection. Stokes (blue) and anti-Stokes (blue) sidebands for the release-free device measured with single-photon detection. Error bars represent standard deviation assuming Poissonian statistics for photon arrival. We place the pump at $\Delta = \pm \omega_{\rm m}$ and measure the optomechanical sideband resonant with the OMC optical mode. By sweeping the resonance frequency of the pump filter stack, we trace out the sideband to find detection rates for thermometry calibration. Finally, we fit the data to Eq. (E4).

filters. When the filters are correctly placed, we couple in the device and SNSPDs to measure $\Gamma_{\pm}(\Delta_p)$ (Fig. 8). To take the pump filter transfer function into account we use that

$$\Gamma_{\pm}(\Delta_{\rm p}) = \Gamma_{\pm} \int_{-\infty}^{\infty} T(\omega)^k \frac{\gamma_{\rm m}/(2\pi)d\omega}{(\omega - \Delta_{\rm p})^2 + (\gamma_{\rm m}/2)^2}. \quad (E4)$$

Here k is the number of filters with transfer function $T(\omega) = (1 + (\omega/\kappa_{\rm pf})^2)^{-1}$ where $\kappa_{\rm pf}$ is the individual pump filter FWHM. For $\gamma_{\rm m} \ll \kappa_{\rm pf}$, Eq. (E4) simplifies to $\Gamma_{\pm}(\Delta_{\rm p}) \approx \Gamma_{\pm} \cdot T(\Delta_{\rm p})^k$.

Due to vacuum fluctuations providing a reference, sideband asymmetry calibration requires less prior knowledge about the optomechanical system. This extra reference makes it an attractive choice when preparing for a thermometry experiment. Crucially, knowledge of the setup detection efficiency η_{tot} allows for calculation of the optomechanical coupling through Eq. (E2). This method can then be cross-referenced with other options for measuring coupling such as EIT. However, the sidebandasymmetry method also comes with complications that have to be taken into account. Firstly, excess laser noise at the mechanical frequency can cause both heating and noise squashing/anti-squashing [43, 45]. In addition, the method assumes equal experimental conditions when reading out both sidebands. When using one laser to read out both sidebands, care has to be taken to guarantee equal $n_{\rm c}$ and $n_{\rm m}$ for both red and blue detuned experiments. Therefore the power of the experiment must be low enough to ensure $\gamma_{\rm om} \ll \gamma_0 + \gamma_{\rm p}$ to not cause excessive optomechanical back-action. Lastly, any error arising from noise or unequal experiment conditions for the two detunings propagates unfavorably when the asymmetry is weak, i.e. at insufficiently low $n_{\rm m}$. Therefore, a proper sideband asymmetry calibration favors devices

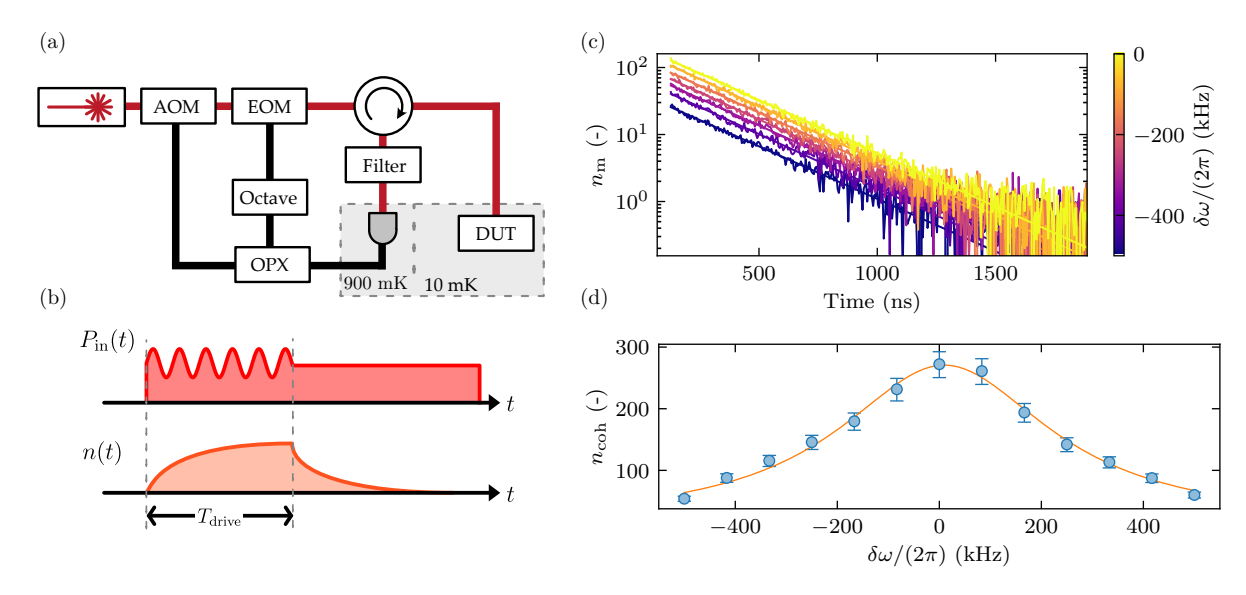


FIG. 9. Thermometry calibration through coherent excitation. (a) Simplified experimental setup. A red detuned optical pulse train is generated using fast Acousto-Optic Modulation (AOM). Part of each pulse is modulated at the mechanical frequency with an amplitude Electro-Optic Modulator (EOM). Pump filters are used to selectively detect the anti-Stokes sideband using single photon detection. A pulse sequencer unit (QM OPX) orchestrates modulation pulsing. The MHz range idler output of the OPX is upconverted into the GHz regime with a local oscillator (QM Octave). (b) Experiment pulse scheme. We excite the OMC optical mode using a red detuned optical pulse train. During an initial time $T_{\rm drive}$, we drive the mechanical mode coherently by modulating the input at the mechanical frequency. After $T_{\rm drive}$, the drive modulation is turned off to detect the free mechanical decay. (c) Free mechanical decay with exponential fits after coherent driving at modulation frequency $\omega_{\rm mod} = \omega_{\rm m} + \delta\omega$. (d) Estimated phonon occupation $(n_{\rm coh})$ at the end of coherent drive (t=0 in (c)) for varying modulation frequencies with least squares standard deviation. Coherently excited phonons follow a Lorentzian around the mechanical frequency $\delta\omega = 0$.

that achieve low $n_{\rm m}$ for high pump powers to achieve higher signal-to-noise ratio. We also note that when using this calibration for pulsed experiments, we perform the calibration with CW excitation first and use the methods described in App. F to extract time-dependent average phonon occupations. Due to the time dynamics of the pump filters, we are not aware of a straightforward sideband-asymmetry calibration method for pulsed experiments when pulse durations are similar to the pump filter rise time.

Coherent excitation. This alternative to sideband asymmetry calibration also relies on a mechanical occupation reference; although this time, the reference is a coherent state with known amplitude. To drive the mechanics into a coherent state of known amplitude, we send an amplitude-modulated optical pulse train to the device. The amplitude modulation is driven at the mechanical frequency such that the optical beat note between pump and modulated sideband coherently drives the mechanics. After the mechanics has been driven during an initial time T_{drive} the modulation is terminated and the anti-Stokes sideband is read out using pump filters and single-photon detectors. During this time, the mechanical mode decays from the elevated coherent state back to the thermal state set by optical absorption.

To calculate the expected coherent amplitude we follow

the derivation given in Ref. [46] to obtain

$$n_{\rm coh} = \frac{4\eta_{\rm o}\gamma_{\rm om}\xi_{\rm sb}\Phi_{\rm pump}}{\gamma_{\rm m}^2}.$$
 (E5)

In this equation, $\xi_{\rm sb}$ is the modulated sideband power relative to the pump and $\Phi_{\rm pump}$ is the pump photon flux in the on-chip bus waveguide. In addition, we assume that the drive pulse is significantly longer than the response time of the mechanics ($\gamma_{\rm m}^{-1} \ll T_{\rm drive}$). The anti-Stokes detection rate measured at $n_{\rm m} = n_{\rm coh}$ ($\Gamma_{\rm m}^{\rm coh}$) now gives the calibration rate

$$\Gamma_{\text{cal}}^{\text{coh}} = \frac{\Gamma_{-}^{\text{coh}}}{n_c n_{\text{coh}}}.$$
 (E6)

We perform the calibration for the release-free device with $T_{\rm drive}=2\,\mu{\rm s}$ long drive pulses and study the mechanical decay for varying drive frequencies (Fig. 9 (c)). As expected, the decay follows an exponential function with a time constant consistent with data presented in Fig. 3d. Due to interference between the anti-Stokes scattered and electro-optic sidebands (EIT), we obtain the detection rate corresponding to the estimated $n_{\rm coh}$ through extrapolation. Using the interference-free part of the exponential decay (Fig. 9c) we estimate the detection rate at the end of the driving pulse (t=0).

In summary, the various calibration techniques presented in this section provide both advantages and drawbacks. Due to being significantly more involved, we use

TABLE II. Results from performing three different methods of calibration for the release-free device. We calculate the uncertainties by propagating estimated error intervals on all ingoing parameters used in Eqs. (E2), (E3), (E6).

Method	$\Gamma_{\rm cal} \ ({\rm cps})$
	24.7 ± 3.5
Sideband asymmetry	$ 21.1 \pm 7.0 $
Coherent excitation	$ 20.8 \pm 2.1 $

coherent excitation calibration sparingly as a cross-check for the less time-consuming options. We therefore calibrate all data presented in the main text of this work with sideband asymmetry. However, we confirm that all calibration methods agree to within the uncertainty set by the ingoing parameters. We present example data of calibration rates measured through the three methods in Tab. II.

Appendix F: Pump filter dynamics in pulsed thermometry

The thermometry experiments in this work are mostly based on the phonon-counting technique described in the Method section of the main text. In this technique, we use tunable narrowband optical filters to extract the desired optomechanical sideband for detection on a singlephoton detector. In our setup, the filter stack comprises a pair of 13.2 MHz bandwidth, 18.8 GHz FSR fiber coupled Fabry-Pérot filters (Stable Laser Systems). The filters are arranged in series and provide $< 2\,\mathrm{dB}$ insertion loss at maximum transmission and 114 dB pump suppression at 5 GHz detuning from resonance. Though essential for the phonon counting measurement technique, the filter stack's bandwidth must be carefully considered when analyzing measurement results. Continuous-wave considerations are well covered in Ref. [17]; however, additional temporal dynamics must also be considered for experiments with short optical pulses.

We base the analysis on the amplitude transfer function for a lossless Fabry–Pérot filter comprising two identical mirrors with reflectivity r given by Yu et al. [47] as

$$t(\omega) = \frac{1 - r}{1 - r \exp(-i2\omega t_0)} e^{-i\omega t_0},$$
 (F1)

where $t_0 = (2 \cdot \text{FSR})^{-1}$ is the optical passage time through the filter. We find the mirror reflectivity r through the relation

$$F = \frac{\pi\sqrt{r}}{1-r},\tag{F2}$$

where F is the filter finesse. This holds for high finesse filters which is the case for our filter stack where $F \approx 1400$. We express the optical input field waveform as $E_{\rm in}(t) = \sqrt{P_{\rm in}(t)} \exp(-i\omega_{\rm sb}t)$, where $\omega_{\rm sb}$ is the sideband

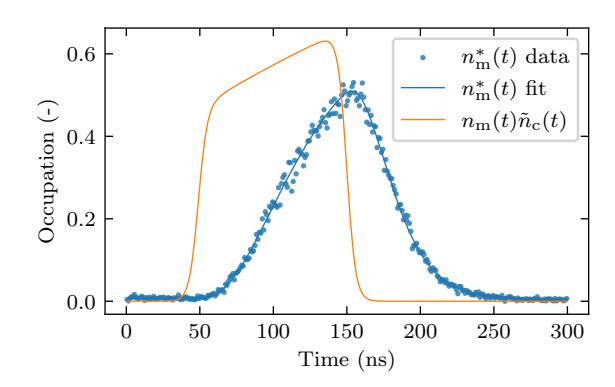


FIG. 10. Filter dynamics compensation. We use the transfer function of the pump filters to derive the pulse-gated thermal occupation $n_{\rm m}(t)\tilde{n}_c(t)$ given calibrated filter output data $n_{\rm m}^*(t)$ measured through single-photon detection. We take data points from Fig. 5c of the main text, representing the anti-Stokes sideband detected when exciting the release-free device with $T_0=100\,{\rm ns}$ pulses detuned to $\Delta=-\omega_{\rm m}$. From the fit, we extract $n_{\rm i}=0.42$ and $n_{\rm f}=1.25$ at a repetition rate of 33 kHz.

frequency and $P_{\rm in}(t)$ is the normalized input power envelope. Now, using Eq. (F1) we get the filter field output as

$$E_{\text{out}}(t) = \mathcal{F}^{-1} \left[\mathcal{F}[E_{\text{in}}] \cdot t(\omega)^k \right],$$
 (F3)

where $\mathcal{F}[\cdot]$ is the Fourier transform and k is the number of identical filters in the stack. To get the normalized power output of the filter stack, we take the absolute square of Eq. (F3) which simplifies when the input signal is resonant with a filter mode (e.g. $\omega_{\rm sb} = \pi/t_0$). A change of variables in the Fourier transform yields

$$P_{\text{out}}(t) = \left| \mathcal{F}^{-1} \left[\mathcal{F} \left[\sqrt{P_{\text{in}}} \right] \cdot t(\omega)^k \right] \right|^2.$$
 (F4)

Next, we use Eqs. (2) and (E2) to connect the dynamics of the filter input optical power to that of the optomechanical occupations $n_{\rm m}, n_{\rm c}$. When omitting $\Gamma_{\rm noise}$ we get

$$P_{\rm in}(t) = \Gamma_{\rm cal} n_{\rm c}^{\rm max} \hbar \omega_{\rm o} (n_{\rm m}(t) + (1 \pm 1)/2) \tilde{n}_{\rm c}(t), \quad (F5)$$

where $\tilde{n}_{\rm c}(t)=n_{\rm c}(t)/n_{\rm c}^{\rm max}$ is the normalized input pulse power. Finally, defining the calibrated SPD signal as $n_{\rm m}^*(t)+(1\pm1)/2=P_{\rm out}(t)/(\Gamma_{\rm cal}n_{\rm c}^{\rm max}\hbar\omega_{\rm o})$ we obtain

$$n_{\rm m}^*(t) + \frac{1}{2}(1 \pm 1) = \left| \mathcal{F}^{-1} \left[\mathcal{F} \left[\sqrt{(n_{\rm m} + (1 \pm 1)/2)\tilde{n}_{\rm c}} \right] \cdot t(\omega)^k \right] \right|^2.$$
 (F6)

In summary, with access to calibrated SPD data $n_{\rm m}^*(t)$, AOM pulse envelop $\tilde{n}_{\rm c}(t)$ and filter transfer function $t(\omega)$, we use Eq. (F6) to infer the phonon occupation dynamics $n_{\rm m}(t)$ and its parameters through Eq. (1). We calibrate

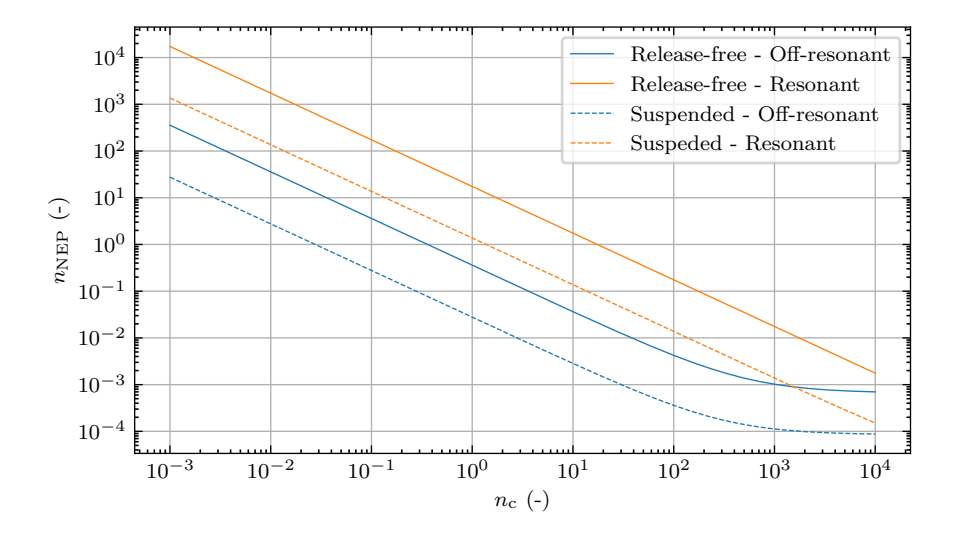


FIG. 11. Noise equivalent phonon occupation. We plot the noise equivalent phonon occupation as a function of optical power given in units of n_c .

the AOM waveform $\tilde{n}_{\rm c}(t)$ by measuring the output of the AOMs directly on our SPD with heavy attenuation.

In Fig. 10, we show an example fit to 100 ns pulsed anti-Stokes sideband data with 33 kHz repetition rate (Fig. 5a,c,e). In this fit, we use a premeasured $\gamma_{\rm m}$ as input parameter and fit the data for $[n_{\rm i}, n_{\rm f}, t_{\rm stop}, n_{\rm NEP}]$. The parameter $t_{\rm stop}$ represents the input pulse stop time and $n_{\rm NEP}$ is the phonon occupation equivalent with the detector dark counts, entering as a constant addition to Eq. (F6). Note that by using Eq. (1) for $n_{\rm m}(t)$, we omit any dynamics in the thermal drive caused by the finite rise-time of the optical pulse. For a more detailed description on our fitting see App. G.

Appendix G: Bayesian fitting methods

Inferring the dynamics of the mechanical mode during optical pulsing is made complicated when the timescale of the filter dynamics is comparable to the dynamics of the mechanical mode occupation. This is generally the case for our release-free device where $\gamma_{\rm m}/\kappa_{\rm pf}>0.01$ with $\kappa_{\rm pf}$ as the FWHM of an individual pump filter. A further complication is that the low photon scattering rate at low powers leads to low amounts of data. Due to the above, the range of model parameter values that are consistent with measured data may be large when the filter transfer functions obfuscate the data. In this work, we use Bayesian parameter estimation and Markov chain Monte Carlo (MCMC) methods to both fit the parameters of our model and, crucially, get an accurate estimate for the uncertainty in our estimation.

Given a model M that takes model parameters θ , collected data D, and prior information I, we seek to infer the posterior probability distribution $p(\theta|D, M, I)$. This

probability can be rewritten using Bayes rule as

$$p(\theta|D, M) = \frac{p(D|\theta, M)p(\theta|M)}{p(D|M)},$$
 (G1)

where we omit I for brevity.

In Eq. (G1), $p(D|\theta, M)$ is the likelihood which model the probability of measuring the data D given certain model parameters θ . In our case, the models for phonon and filter dynamics along with system losses give a predicted photon detection rate during the extent of a pulse $\Gamma_{\theta}(t)$ (see Eq. (2) and App. F). During an SPD measurement, we collect clicks into time bins of size Δt . When assuming Poissonian statistics for incoming photon clicks, the probability of measuring k_i clicks in the time bin $[t_i, t_i + \Delta t]$ is

$$p_i(k_i) = \frac{\lambda_i^{k_i} e^{-\lambda}}{k_i!},\tag{G2}$$

where $\lambda_i = \Gamma_{\theta}(t_i)\Delta t$. Therefore, we get the likelihood as the probability of measuring the data D, consisting of counts k_1, k_2, \ldots, k_N in time bins t_1, t_2, \ldots, t_N through

$$p(D|\theta, M) = \prod_{i=1}^{N} p_i.$$
 (G3)

Next, the factor $p(\theta|M)$ in Eq. (G1) encapsulates the prior beliefs on ingoing parameters which we choose as uniform distributions over sensible values. Finally, we consider the evidence of the model, p(D|M), as an inconsequential normalization constant due to its independence on θ .

To analyze the posterior distribution, we use MCMC methods, specifically the emcee python package [48], which optimizes the likelihood for θ and samples the posterior distribution $p(\theta|D, M)$. We get credibility intervals

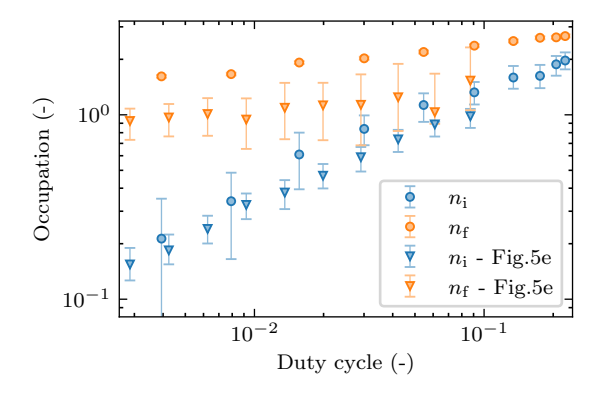


FIG. 12. Thermal noise limit duty cycle dependence. Initial (n_i) and final (n_f) occupation data from pump-probe experiment without coherent driving. In this experiment, pump and probe pulse durations are $2 \mu s$, $n_c = 324$ and $T_d = 10 \mu s$. We vary the duty cycle of the experiment by controlling the delay between pulse pairs. In addition, we plot occupation data from Fig. 5e. Data is presented with 95% credibility intervals.

for each parameter in the model by taking appropriate quantiles of the marginalized distribution. This ensures that the uncertainty in any nuisance parameters are properly propagated to the uncertainty of the parameters of interest.

Appendix H: Noise equivalent phonon occupation

After proper thermometry calibration (App. E), we can estimate the noise equivalent phonon occupation $(n_{\rm NEP})$ which serves as a soft lower limit to the measurable phonon occupation for any given experiment. We assume that the noise measured during SPD comes primarily from two sources; detection events in the absence of laser light (commonly referred to as dark counts) and excess laser noise. Dark counts include internally generated detector clicks, black-body radiation and stray light from e.g. laboratory lighting. The excess laser noise stems either from light at the pump frequency not perfectly attenuated by the pump filters or from laser noise process' at the mechanical frequency such as laser phase noise [43].

We measure the excess laser noise by first aligning the pump filter stack to be detuned from the pump laser by the mechanical frequency. Next, we redirect the pump laser to bypass the device and directly detect its transmission through the pump filters. Without pre-filtering of the pump laser, we measure a photon flux on the SPD equivalent to $-92\,\mathrm{dBc}$ before the pump filters. This noise is likely dominated by phase noise and spontaneous emission induced amplitude noise. When engaging pump pre-filtering, the measured noise photon flux drops to $-113.6\,\mathrm{dBc}$. This number is consistent with the $114\,\mathrm{dB}$ expected pump suppression given by Eq. (F1) as-

suming two filters with FWHM = $13.2\,\mathrm{MHz}$ and FSR = $18.8\,\mathrm{GHz}$.

Now, the noise equivalent phonon occupation is given by the ratio between expected noise photons and the calibration rate at given n_c . This ratio differs depending on the detuning and is given by [15]

$$n_{\text{NEP}}|_{\Delta=\pm\omega_{\text{m}}} = \frac{\Gamma_{\text{DCR}}}{\Gamma_{\text{cal}}n_{\text{c}}} + A\left(\frac{\kappa\omega_{\text{m}}}{2\kappa_{\text{e}}g_{\text{om}}}\right)^{2}, \tag{H1}$$

$$n_{\text{NEP}}|_{\Delta=0} = \frac{\Gamma_{\text{DCR}}}{\Gamma_{\text{cal}}n_{\text{c}}} \left(\frac{2\omega_{\text{m}}}{\kappa}\right)^{2} + A\left(\frac{\kappa\omega_{\text{m}}(1-2\eta_{\text{o}})}{\kappa_{\text{e}}g_{\text{om}}}\right)^{2}, \tag{H2}$$

where $\Gamma_{\rm DCR}$ is the detected dark count rate and A is the pump suppression. We plot the expected $n_{\rm NEP}$ for both release-free and suspended devices in Fig. 11. In the experiments with our release-free device, we are mainly limited by dark count noise $\Gamma_{\rm DCR} \approx 7\,{\rm Hz}$ and fiber-chip coupling $\eta_{\rm fc} \approx 0.1$. We expect that with reasonable setup improvements, $\Gamma_{\rm cal}$ can be improved by more than 5 dB giving the same improvement in $n_{\rm NEP}$.

Appendix I: Slow decaying reservoir dynamics

In Sec. VI, we study the ringdown of a coherently excited mechanical occupation and find that after an initial time governed by intrinsic mechanical decay (γ_0), a noise floor at $n_{\rm m}\approx 0.8$ limits further drop in thermal noise for $T_{\rm d}>2\,\mathrm{\mu s}$ (Fig. 3f). In that experiment the repetition rate was fixed at $R=70\,\mathrm{kHz}$. In this section, we show that this measured noise floor can be decreased by decreasing the average optical power supplied to the device

We now run another pump-probe experiment with 2 µs pulse durations, although this time we remove the EOM driving to exclude the possibility of the noise floor originating from EOM noise at the mechanical frequency. The power of the experiment is set to be $n_c = 324$ and $T_{\rm d} = 10 \,\mu s$ while the delay between pulse pairs is varied, effectively controlling the experiment's repetition rate. We proceed to fit the data of the probe pulse and extract n_i and n_f as function of the duty cycle of the experiment; i.e., the fractional experiment time when optical power is on, including both pump and probe pulses. We see a clear reduction in both n_i and n_f for lower duty cycle pulse trains (Fig. 12). In addition, we see a dutycycle dependence in the ratio n_i/n_f , suggesting that the reservoirs decay dynamics and coupling to the mechanical mode also depend on average dissipated optical power.

The observed duty-cycle dependence of initial and final occupations is reminiscent of the short pulse noise from Sec. VI. By plotting the data from Fig. 3e together with the data from this pump-probe experiment we see good agreement in the behavior of n_i as a function of duty cycle (Fig. 12). We thus conclude that the thermal noise decay measured in Fig. 3e is limited by the dynamics

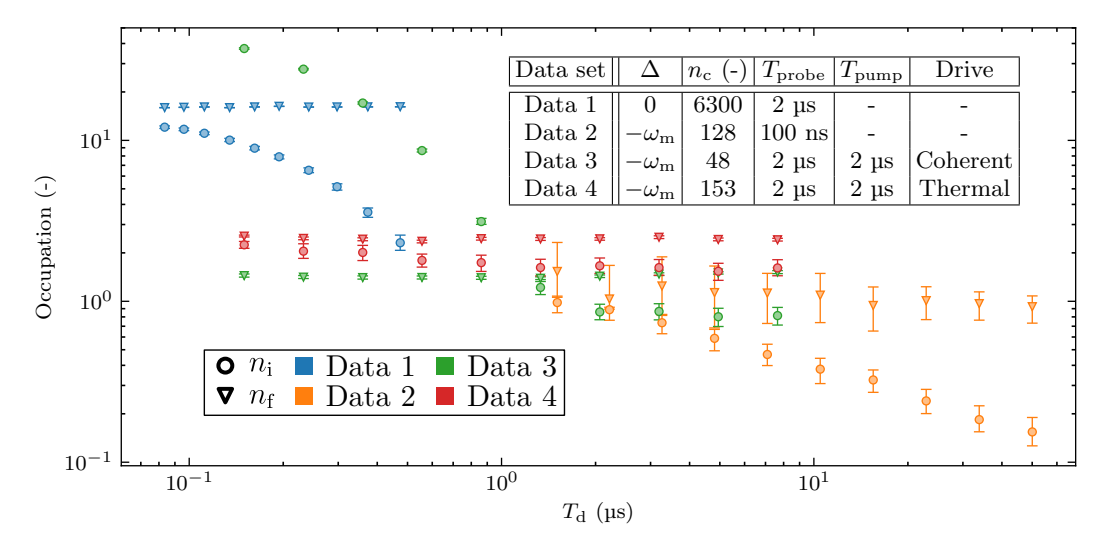


FIG. 13. Overview of release-free data. Release-free mechanical occupation measured in the pulsed experiments throughout this study. We take Data 1 from Fig. 3d, Data 2 from Fig. 5e, and Data 3 from Fig. 5f. Data 4 represents a pump-probe $T_{\rm d}$ sweep with no coherent drive during the pump pulse. For Data 1 and 2, $T_{\rm d}$ refers to the downtime between subsequent pulses, whilst it refers to the delay between pump and probe for Data 3 and 4.

of the measured background in Fig. 3f. Given the non-exponential nature of pulse noise as function of repetition rate reported for two-dimensional OMCs [4], we conjecture that this measured noise source is not unique to the release-free platform. In conclusion, we believe that further understanding of the source of this noise is crucial for future development of fast and low noise operation regardless of optomechanical system type.

Appendix J: Compiled release-free ringdown

For ease of overview, we report on all pulsed ring-down experiments performed throughout this work (Fig. 13). We also present a thermally-driven pump-probe experiment to check that the noise floor measured in Fig. 5f is not caused by residual EOM noise at the mechanical frequency. We perform the experiment identically to Fig. 5b except having the EOM switched out of the laser path and increasing the power to $n_{\rm c}=153$. For this experiment, we immediately observe the slow decay dynamics in $n_{\rm i}$ from $T_{\rm d}>2\,\rm \mu s$, ruling out the EOM as the source of the noise floor in Fig. 5f.

- [1] A. H. Safavi-Naeini, D. V. Thourhout, R. V. Laer, and R. Baets, Controlling phonons and photons at the wavelength scale: integrated photonics meets integrated phononics, Optica, Vol. 6, Issue 2, pp. 213-232 6, 213 (2019), publisher: Optical Society of America.
- [2] C.-L. Zou, H. X. Tang, L. Jiang, W. Fu, X. Han, H. X. Tang, and H. X. Tang, Microwave-optical quantum frequency conversion, Optica, Vol. 8, Issue 8, pp. 1050-1064 8, 1050 (2021), publisher: Optical Society of America.
- [3] J. Chan, T. P. M. Alegre, A. H. Safavi-Naeini, J. T. Hill, A. Krause, S. Gröblacher, M. Aspelmeyer, and O. Painter, Laser cooling of a nanomechanical oscillator into its quantum ground state, Nature 2011 478:7367 478, 89 (2011), publisher: Nature Publishing Group.
- [4] F. M. Mayor, S. Malik, A. G. Primo, S. Gyger, W. Jiang, T. P. M. Alegre, and A. H. Safavi-Naeini, High photonphonon pair generation rate in a two-dimensional optomechanical crystal, Nature Communications 16, 2576 (2025), publisher: Nature Publishing Group.

- [5] L. Qiu, I. Shomroni, P. Seidler, and T. J. Kippenberg, Laser Cooling of a Nanomechanical Oscillator to Its Zero-Point Energy, Physical Review Letters 124, 173601 (2020).
- [6] W. Jiang, F. M. Mayor, S. Malik, R. Van Laer, T. P. McKenna, R. N. Patel, J. D. Witmer, and A. H. Safavi-Naeini, Optically heralded microwave photon addition, Nature Physics , 1 (2023), publisher: Nature Publishing Group.
- [7] S. Meesala, S. Wood, D. Lake, P. Chiappina, C. Zhong, A. D. Beyer, M. D. Shaw, L. Jiang, and O. Painter, Nonclassical microwave—optical photon pair generation with a chip-scale transducer, Nature Physics 20, 871 (2024), publisher: Nature Publishing Group.
- [8] R. Riedinger, A. Wallucks, I. Marinković, C. Löschnauer, M. Aspelmeyer, S. Hong, and S. Gröblacher, Remote quantum entanglement between two micromechanical oscillators, Nature 556, 473 (2018), publisher: Nature Publishing Group.

- [9] R. Riedinger, S. Hong, R. A. Norte, J. A. Slater, J. Shang, A. G. Krause, V. Anant, M. Aspelmeyer, and S. Gröblacher, Non-classical correlations between single photons and phonons from a mechanical oscillator, Nature 530, 313 (2016), publisher: Nature Publishing Group.
- [10] S. Hong, R. Riedinger, I. Marinković, A. Wallucks, S. G. Hofer, R. A. Norte, M. Aspelmeyer, and S. Gröblacher, Hanbury Brown and Twiss interferometry of single phonons from an optomechanical resonator, Science 358, 203 (2017), publisher: American Association for the Advancement of Science.
- [11] L. Chen, A. R. Korsch, C. M. Kersul, R. Benevides, Y. Yu, T. P. M. Alegre, and S. Gröblacher, Bandwidthtunable Telecom Single Photons Enabled by Low-noise Optomechanical Transduction (2024), arXiv:2410.10947 [quant-ph].
- [12] G. S. MacCabe, H. Ren, J. Luo, J. D. Cohen, H. Zhou, A. Sipahigil, M. Mirhosseini, and O. Painter, Nanoacoustic resonator with ultralong phonon lifetime, Science 370, 840 (2020), publisher: American Association for the Advancement of Science.
- [13] G. Huang, A. Beccari, N. J. Engelsen, and T. J. Kippenberg, Room-temperature quantum optomechanics using an ultralow noise cavity, Nature 626, 512 (2024), publisher: Nature Publishing Group.
- [14] S. M. Meenehan, J. D. Cohen, S. Gröblacher, J. T. Hill, A. H. Safavi-Naeini, M. Aspelmeyer, and O. Painter, Silicon optomechanical crystal resonator at millikelvin temperatures, Physical Review A 90, 011803 (2014), publisher: American Physical Society.
- [15] S. M. Meenehan, J. D. Cohen, G. S. MacCabe, F. Marsili, M. D. Shaw, and O. Painter, Pulsed Excitation Dynamics of an Optomechanical Crystal Resonator near Its Quantum Ground State of Motion, Physical Review X 5, 041002 (2015), publisher: American Physical Society.
- [16] H. Ren, M. H. Matheny, G. S. MacCabe, J. Luo, H. Pfeifer, M. Mirhosseini, and O. Painter, Twodimensional optomechanical crystal cavity with high quantum cooperativity, Nature Communications 2020 11:1 11, 1 (2020), publisher: Nature Publishing Group.
- [17] S. Sonar, U. Hatipoglu, S. Meesala, D. P. Lake, H. Ren, and O. Painter, High-efficiency low-noise optomechanical crystal photon-phonon transducers, Optica 12, 99 (2025), publisher: Optica Publishing Group.
- [18] H. M. Doeleman, T. Schatteburg, R. Benevides, S. Vollenweider, D. Macri, and Y. Chu, Brillouin optomechanics in the quantum ground state, Physical Review Research 5, 043140 (2023).
- [19] J. Kolvik, P. Burger, J. Frey, and R. V. Laer, Clamped and sideband-resolved silicon optomechanical crystals, Optica 10, 913 (2023), publisher: Optica Publishing Group.
- [20] P. Burger, J. Frey, J. Kolvik, D. Hambraeus, and R. Van Laer, Design of a release-free piezooptomechanical quantum transducer, APL Photonics 10, 010801 (2025).
- [21] P. E. Lagasse, Higher-order finite-element analysis of topographic guides supporting elastic surface waves, The Journal of the Acoustical Society of America 53, 1116 (1973).
- [22] M. Borselli, T. J. Johnson, and O. Painter, Measuring the role of surface chemistry in silicon microphotonics, Applied Physics Letters 88, 131114 (2006), publisher:

- American Institute of PhysicsAIP.
- [23] J. Chen, X. Xu, J. Zhou, and B. Li, Interfacial thermal resistance: Past, present, and future, Reviews of Modern Physics 94, 025002 (2022), publisher: American Physical Society.
- [24] T. Zeng and G. Chen, Phonon Heat Conduction in Thin Films: Impacts of Thermal Boundary Resistance and Internal Heat Generation, Journal of Heat Transfer 123, 340 (2000).
- [25] J. Chan, A. H. Safavi-Naeini, J. T. Hill, S. Meenehan, and O. Painter, Optimized optomechanical crystal cavity with acoustic radiation shield, Applied Physics Letters 101, 081115 (2012), publisher: American Institute of PhysicsAIP.
- [26] A. H. Safavi-Naeini, T. P. M. Alegre, J. Chan, M. Eichenfield, M. Winger, Q. Lin, J. T. Hill, D. E. Chang, and O. Painter, Electromagnetically induced transparency and slow light with optomechanics, Nature 472, 69 (2011), number: 7341 Publisher: Nature Publishing Group.
- [27] P. E. Barclay, K. Srinivasan, and O. Painter, Nonlinear response of silicon photonic crystal microresonators excited via an integrated waveguide and fiber taper, Optics Express 13, 801 (2005), publisher: Optica Publishing Group.
- [28] J. Komma, C. Schwarz, G. Hofmann, D. Heinert, and R. Nawrodt, Thermo-optic coefficient of silicon at 1550 nm and cryogenic temperatures, Applied Physics Letters 101, 041905 (2012).
- [29] M. Aspelmeyer, T. J. Kippenberg, and F. Marquardt, Cavity optomechanics, Reviews of Modern Physics 86, 1391 (2014), publisher: American Physical Society.
- [30] A. Y. Cleland, E. A. Wollack, and A. H. Safavi-Naeini, Studying phonon coherence with a quantum sensor, Nature Communications 15, 4979 (2024), publisher: Nature Publishing Group.
- [31] M. Chen, J. C. Owens, H. Putterman, M. Schäfer, and O. Painter, Phonon engineering of atomic-scale defects in superconducting quantum circuits, Science Advances 10, eado6240 (2024), publisher: American Association for the Advancement of Science.
- [32] L.-M. Duan, M. D. Lukin, J. I. Cirac, and P. Zoller, Longdistance quantum communication with atomic ensembles and linear optics, Nature 414, 413 (2001), publisher: Nature Publishing Group.
- [33] S. Krastanov, H. Raniwala, J. Holzgrafe, K. Jacobs, M. Lončar, M. J. Reagor, and D. R. Englund, Optically Heralded Entanglement of Superconducting Systems in Quantum Networks, Physical Review Letters 127, 040503 (2021).
- [34] T. H. Haug, A. F. Kockum, and R. Van Laer, Heralding entangled optical photons from a microwave quantum processor, Physical Review Applied 22, 034068 (2024), publisher: American Physical Society.
- [35] S. Kono, J. Pan, M. Chegnizadeh, X. Wang, A. Youssefi, M. Scigliuzzo, and T. J. Kippenberg, Mechanically induced correlated errors on superconducting qubits with relaxation times exceeding 0.4 ms, Nature Communications 15, 3950 (2024), publisher: Nature Publishing Group.
- [36] H. Zhao, W. D. Chen, A. Kejriwal, and M. Mirhosseini, Quantum-enabled microwave-to-optical transduction via silicon nanomechanics, Nature Nanotechnology 20, 602 (2025), publisher: Nature Publishing Group.

- [37] R. Sahu, L. Qiu, W. Hease, G. Arnold, Y. Minoguchi, P. Rabl, and J. M. Fink, Entangling microwaves with light, Science 380, 718 (2023), publisher: American Association for the Advancement of Science.
- [38] F. Lecocq, F. Quinlan, K. Cicak, J. Aumentado, S. A. Diddams, and J. D. Teufel, Control and readout of a superconducting qubit using a photonic link, Nature 591, 575 (2021), number: 7851 Publisher: Nature Publishing Group.
- [39] T. C. van Thiel, M. J. Weaver, F. Berto, P. Duivestein, M. Lemang, K. L. Schuurman, M. Žemlička, F. Hijazi, A. C. Bernasconi, C. Ferrer, E. Cataldo, E. Lachman, M. Field, Y. Mohan, F. K. de Vries, C. C. Bultink, J. C. van Oven, J. Y. Mutus, R. Stockill, and S. Gröblacher, Optical readout of a superconducting qubit using a piezooptomechanical transducer, Nature Physics, 1 (2025), publisher: Nature Publishing Group.
- [40] G. Arnold, T. Werner, R. Sahu, L. N. Kapoor, L. Qiu, and J. M. Fink, All-optical superconducting qubit readout, Nature Physics , 1 (2025), publisher: Nature Publishing Group.
- [41] R. D. Delaney, M. D. Urmey, S. Mittal, B. M. Brubaker, J. M. Kindem, P. S. Burns, C. A. Regal, and K. W. Lehnert, Superconducting-qubit readout via low-backaction electro-optic transduction, Nature 606, 489 (2022), publisher: Nature Publishing Group.
- [42] J. D. Cohen, S. M. Meenehan, G. S. MacCabe, S. Gröblacher, A. H. Safavi-Naeini, F. Marsili, M. D. Shaw, and O. Painter, Phonon counting and intensity in-

- terferometry of a nanomechanical resonator, Nature **520**, 522 (2015), publisher: Nature Publishing Group.
- [43] A. H. Safavi-Naeini, J. Chan, J. T. Hill, S. Gröblacher, H. Miao, Y. Chen, M. Aspelmeyer, and O. Painter, Laser noise in cavity-optomechanical cooling and thermometry, New Journal of Physics 15, 035007 (2013), publisher: IOP Publishing.
- [44] J. Chan, Laser cooling of an optomechanical crystal resonator to its quantum ground state of motion, Ph.D. thesis, California Institute of Technology (2012).
- [45] T. J. Kippenberg, A. Schliesser, and M. L. Gorodetsky, Phase noise measurement of external cavity diode lasers and implications for optomechanical sideband cooling of GHz mechanical modes, New Journal of Physics 15, 015019 (2013), publisher: IOP Publishing.
- [46] M. B. Kristensen, N. Kralj, E. C. Langman, and A. Schliesser, Long-lived and Efficient Optomechanical Memory for Light, Physical Review Letters 132, 100802 (2024), publisher: American Physical Society.
- [47] J. Yu, S. Yuan, J.-Y. Gao, and L. Sun, Optical pulse propagation in a Fabry–Perot etalon: analytical discussion, Journal of the Optical Society of America A 18, 2153 (2001).
- [48] D. Foreman-Mackey, D. W. Hogg, D. Lang, and J. Goodman, emcee: The MCMC Hammer, Publications of the Astronomical Society of the Pacific 125, 306 (2013), publisher: IOP Publishing.